LBNL Deliverable to the
Big Sky Carbon Sequestration Partnership:

Milestone Report

Summary of Site Characterization, Data Collection and Review, Development of Static Geologic Model, and Preliminary Multiphase Flow and Reactive Transport Modeling Activities

Quanlin Zhou
Curtis M. Oldenburg
Nicolas Spycher
Lehua Pan
Abdullah Cihan

Earth Sciences Division
Lawrence Berkeley National Laboratory

July 26, 2013
Revised: December 6, 2013

ABSTRACT

This milestone report summarizes LBNL activities for site characterization, data collection and review, development of a static geologic model, preliminary multiphase flow modeling of injection and production, geochemical and reactive transport modeling, and modeling in support of Area of Review (AoR).

LBNL reviewed and used site-characterization data from BSCSP partners to develop a 3D multiphase flow model to simulate two-phase CO_2-brine flow, and to investigate the responses of CO_2 saturation and pressure buildup to CO_2 injection into middle Duperow at Kevin Dome. The simulation results show that limitations to CO_2 injectivity, attributed to low permeability and small CO_2 relative permeability, are a concern for the project. Simulations also show that pressure buildup can be managed, to some extent, by gradually increasing the injection rate to compensate for dynamic relative-permeability effects. Preliminary coupled wellbore-reservoir simulations of CO_2 production flow tests show that single-well production at rates near the 8 kg/s (1 Mt/4 yrs) design rate for 60 days produce a pressure signal that penetrates ~500 m into the dome. The location of the gas-water contact, a current unknown, strongly controls CO_2 production, as does the mobility of water, which depends on uncertain capillary pressure and relative permeability properties of the Duperow production zone. Geochemical equilibrium modeling using an initially steady-state rock-brine geochemical system, based on mineralogy and fluid chemistry derived from published reports and databases, indicates that the brine+CO_2 mixture quickly attains equilibrium with all primary rock minerals, reaching a nearly constant pH near 5 and showing low reactivity with minerals present (and essentially no change in porosity).

Reactive transport modeling of the CO_2 injection process, including full kinetics of the reactions, agrees well with the geochemical equilibrium modeling. Specifically, calcite and dolomite show minor dissolution, but the overall conclusion to date is that reactivity with injected CO_2 is very low, with essentially no CO_2 mineralization predicted. The lack of significant reactivity is attributed to the self-limiting behavior of carbonate dissolution by CO_2, which at elevated calcium concentrations keeps pH to values that are too low for secondary phases to form.

Because of the relative overpressure in the Duperow at Kevin Dome, the project may need to apply the approaches mentioned in the 2013 revised EPA Class VI guidance to define the Area of Review. Analytical solutions of brine pressurization and associated flow up leaky wells show that incremental flow rates for leaky wells located 6 km and 4 km from the injection well are at most approximately 20% and 30% greater, respectively, than hypothetical baseline leakage rates.

TABLE OF CONTENTS

LIST OF TABLES

LIST OF FIGURES

1. EXECUTIVE SUMMARY

The Phase III project of the Big Sky Carbon Sequestration Partnership (BSCSP) at Kevin Dome, Montana, is aimed at understanding the potential of the structural domes in the northwestern part of North America for large-scale geologic carbon sequestration. The BSCSP Phase III project entails producing CO_2 from one of these large structures (Kevin Dome), transporting the CO_2 several miles by pipeline, and injecting it into the brine-filled flank of the dome. The test will help determine the suitability of these kinds of reservoirs for large-scale geologic carbon sequestration, and the potential of these natural CO_2 reservoirs as a source for CO_2-Enhanced Oil Recovery (EOR).

In this project, LBNL supports the BSCSP in its Kevin Dome Phase III project with (1) multiphase flow, reactive geochemical, and hydrogeomechanical numerical modeling; (2) monitoring design, deployment, data analysis, and modeling in both surface and subsurface regions, as needed; and (3) laboratory experiments and measurements for the core of relative permeability and seismic wave propagation. The objective of LBNL's proposed work is to assist BSCSP in carrying out its Phase III project in a safe and environmentally responsible manner, while also achieving the scientific and technical objectives of the project.

This milestone report summarizes LBNL activities on site characterization, data collection and review, development of a static geologic model, preliminary multiphase flow modeling of injection and production, geochemical and reactive transport modeling, and modeling in support of Area of Review (AoR). Through these activities for the pre-injection project phase, LBNL accomplished its objective by providing the project team with predictions of pressure rise, CO_2 saturation, brine migration, geochemical reactions, production responses, AoR analyses, and combinations of these processes, on the basis of existing data. These results form the basis of the ongoing design of the injection, including well locations and monitoring approaches.

In Section 2, we summarize LBNL activities in site characterization, data collection and review, and development and use of the static geologic model. LBNL obtained site-characterization data from BSCSP partners, reviewed these data, and then informed our partners about what was needed for modeling and simulation from the 3D static geologic model. LBNL also reviewed the transferred 3D geologic model in support of our modeling activities. In addition, LBNL independently collected geochemical data on mineralogy and brine chemistry relevant to the project site from the literature and a USGS database.

Section 3 summarizes the development of a 3D multiphase flow model for CO_2 injection, based on the 3D geological model provided by Schlumberger, including determination of the 50 km × 40 km model domain, 2D and 3D mesh generation, and specification of initial and boundary conditions. Three cases of rock properties and two cases of injection schemes were simulated using TOUGH2-MP/ECO2N. In all cases, homogeneity with each unit was assumed because of limited available data on rock properties. All of these simulations were conducted to simulate two-phase CO_2-brine flow and to investigate the responses of CO_2 saturation and pressure buildup to CO_2 injection into middle Duperow. The simulation results in the base case (i.e., the middle Duperow has a porosity of 0.08 and a permeability of 30 md) show cause for concern regarding CO_2 injectivity, because the maximum pressure buildup is higher than the assumed allowable (fracturing) pressure increase of 90 bar. The significant pressure buildup can be

attributed to the low permeability and relatively small CO_2 relative permeability in the two-phase CO_2-brine zone. When the permeability is increased to 80 md at constant porosity, the injectivity issue disappears during the four years of injection. Simulation results for the two injection schemes indicate that the step-rate injection strategy can reduce pressure buildup and thus enhance CO_2 injectivity to a certain degree, by gradually increasing the injection rate to compensate for dynamic relative permeability.

In Section 4, we present preliminary three-dimensional multiphase coupled wellbore-reservoir simulations to investigate questions surrounding CO_2 production from the middle Duperow at Kevin Dome. The simulation domain is a subdomain of the larger Kevin Dome grid discretized to include a 5.5-inch production well screened in the middle Duperow. Production flow tests show that single-well flow at rates near the 8 kg/s (1 Mt/4 yrs) design rate for 60 days produce a pressure signal that penetrates ~500 m into the dome. Production tests over a few days cause pressure to penetrate between 100 and 200 m into the middle Duperow. Higher reservoir permeability enhances deliverability, as expected. The location of the gas-water contact strongly controls CO_2 production, with shallower gas-water contact causing larger pressure drawdown for a given flow rate owing to the reduced gas volume of the reservoir. Potentially a much more serious concern is that a high gas-water contact could cause brine upconing into the well. Our preliminary simulations also suggest that mobility of water is an important factor affecting the productivity, which implies that information on capillary pressure and relative permeability, along with *in situ* water saturation in the gas reservoir, may be important parameters for accurately simulating CO_2 production.

Section 5 reports on geochemical and reactive transport modeling of CO_2 injection into representative model rock and pore-fluid systems. The initial chemical conditions based on these compositions were verified to remain stable for a period of at least 100 years, an important prerequisite for reactive transport simulations to ensure that water-rock interactions predicted during the period of CO_2 injection are related only to the effects of added CO_2, and not to fictitious transient effects. Published thermodynamic databases and kinetic models, along with standard assumptions about mineral surface areas, were used to define kinetic controls on mineral dissolution and precipitation. Preliminary equilibrium geochemical modeling indicates that the brine+CO_2 mixture quickly attains equilibrium with all primary rock minerals, reaching a nearly constant pH near 5 and showing low reactivity with minerals present and essentially no change in porosity. Reactive flow and transport modeling of the CO_2 injection process including full kinetics of the reactions agrees well with the geochemical equilibrium modeling and shows that the pH quickly drops to values near 4.9, and remains near this value for at least 100 years within a horizontal distance of about 500 m from the injection point. Calcite and dolomite show minor dissolution, and the resulting increase in dissolved calcium concentrations drives the precipitation of anhydrite. However, the amount of dissolution and precipitation of these minerals is very small ($< 10^{-4}$ volume fraction change). The overall conclusion based on available information and our geochemical modeling to date is that reactivity is very low, with essentially no CO_2 mineralization predicted. The lack of significant reactivity is attributed to the self-limiting behavior of carbonate dissolution by CO_2, which, at elevated calcium concentrations, keeps pH to values that are too low for secondary phases to form.

Section 6 describes the modeling and analysis of AoR. Because of the apparent pre-injection relative overpressure condition present at Kevin Dome, it appears the project will need to apply the approaches mentioned on p. 42 of the revised EPA Class VI guidance to arrive at an acceptable AoR. To support the estimation of AoR, we carried out modeling using published analytical solutions to single-phase flow equations to calculate brine pressurization and associated flow up (single) leaky wells located at a range of distances from the injection well. We find that the incremental flow rates for hypothetical leaky wells located 6 km and 4 km from the injection well are at most ~20% and 30% greater, respectively, than hypothetical baseline leakage rates. If total brine leakage is considered, and depending on how incremental total leakage is calculated, we find that incremental total leakage can be either a few percent or up to 40% greater (at most) than baseline total leakage.

2. SITE CHARACTERIZATION AND STATIC GEOLOGIC MODEL

The Big Sky Carbon Sequestration Partnership (BSCSP) is conducting the Phase III Geologic Carbon Sequestration (GCS) project at Kevin Dome in north central Montana. Montana State University (MSU), Vecta, and Schlumberger (SLB) have collected data for site characterization (e.g., well locations and logs, 2D seismic surveys, and *in situ* conditions), comprehensively reviewed these data, and then constructed a 3D static geologic model. These data and the geologic model were transferred to LBNL for further analysis in support of modeling and simulation activities. In addition, LBNL independently collected geochemical data on mineralogy and brine chemistry relevant to the project site from the literature and a USGS database.

2.1. Site Characterization

Site characterization at Kevin Dome was mainly conducted by MSU, Vecta, and SLB (Bowen, 2012). LBNL has obtained data from these project partners in support of our modeling efforts. Here, we briefly give some background on the site characterization, which is relevant to the LBNL modeling effort.

Figure 2.1-1 shows the project site at Kevin Dome in north central Montana. The injection site is ~14 km from the U.S.-Canada border. Figure 2.1-2 shows the geologic structures in Montana. There are two relevant features not indicated explicitly in the figures, namely Kevin Dome itself and Sweetgrass Hills to the northeast of the project site.

Figure 2.1-1. *Location of the Kevin Dome project site in north central Montana (Bowen, 2012)*
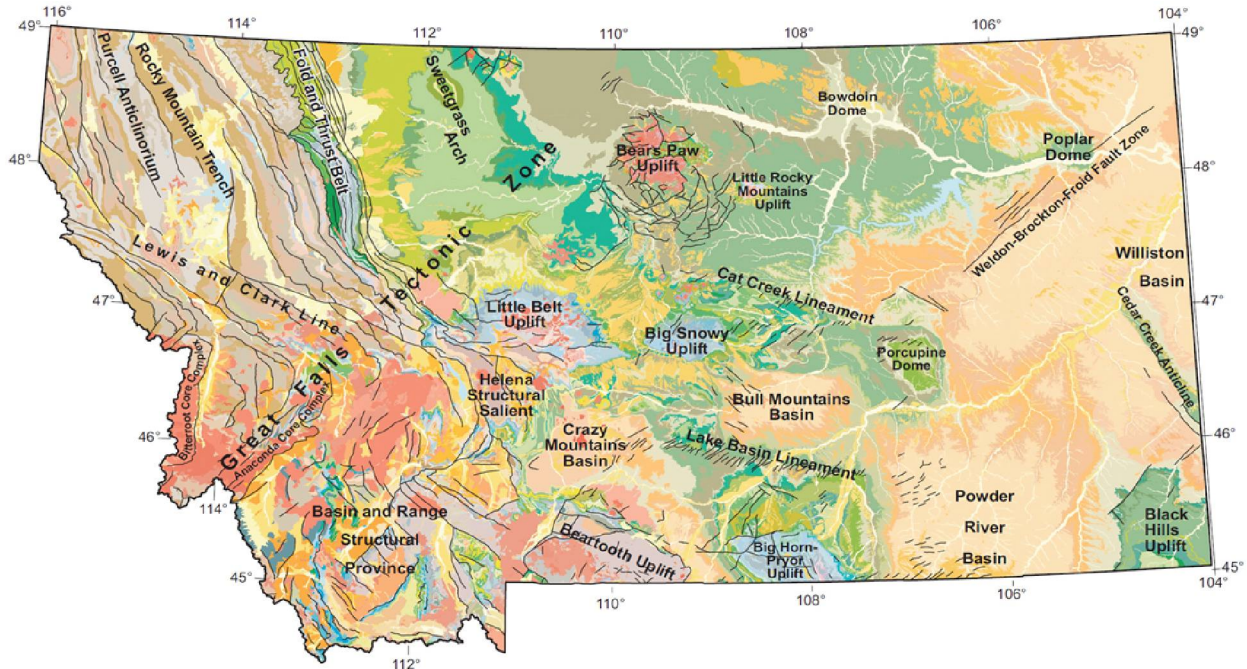
Figure 2.1-2. *Geologic structures in Montana and the nearby Kevin Dome and Sweetgrass Hills close to the project site (Bowen, 2012)*

Figure 2.1-3 shows the stratigraphic column at Kevin Dome. Relevant to LBNL modeling are the Madison, Banff, Bakken, Three Forks, Potlach, Nisku, Duperow, Souris River, and Cambrian formations. The Madison is the deepest Underground Source of Drinking Water (USDW) (see Section 6), and the Nisku, Duperow, and Souris River formations are parts of the storage system used in LBNL multiphase flow modeling (see Sections 3 and 4).
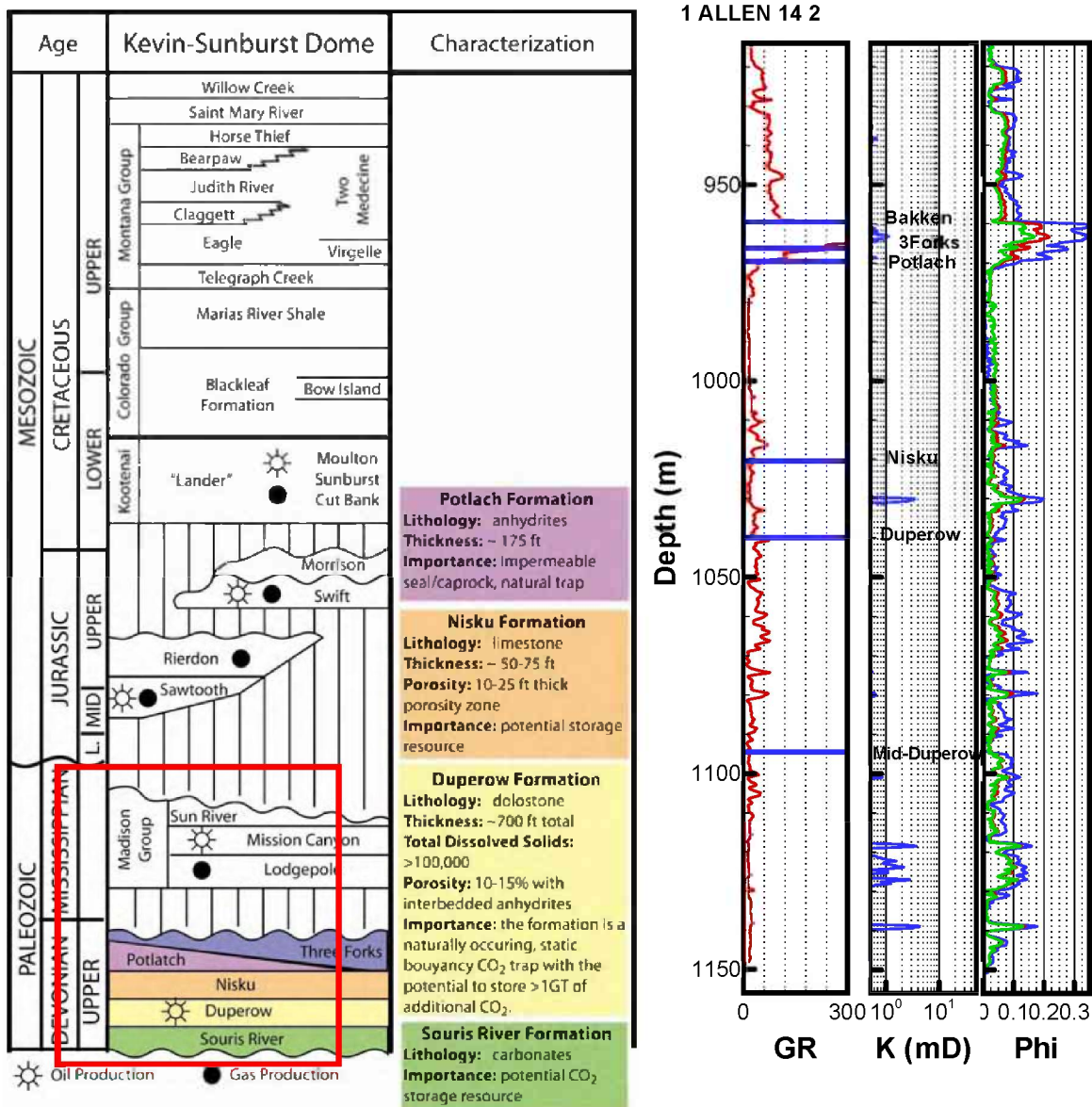
Figure 2.1-3. *Left-hand side: geologic column at Kevin Dome (Bowen, 2012) with the red box showing the relevant formations to the geologic model, USDW, and the storage system for modeling. Right-hand side: a representative well with geophysical logs of gamma ray, calculated intrinsic permeability, and neutron, total, and effective porosity, and the formation tops for formations relevant to LBNL modeling.*

2.2. Data Collection and Review

2.2.1. Hydrogeologic Data

We obtained geophysical logs in LAS (Log ASCII Standard) format for 31 wells near the project site. The geophysical logs include gamma ray, neutron porosity, total porosity, effective porosity, and calculated intrinsic permeability, as well as for other physical variables. We also obtained the formation tops for all the wells (see Figure 2.1-3, right-hand side). Note that all of the calculated permeabilities from well log information appear to be smaller than reasonably

expected, and thus we did not rely on these permeability data in the modeling. To better understand the trend of variability of porosity of the middle Duperow, we grouped the 12 nearby wells into three groups: the east group (J Fey 33-33, True State, Kolstad, and Johannsen 1), the nearby group (Allen, LIoyd Danielson 2, Leonard Bashor 1, Tordale 33-21, and State Carden 1) and the west group (Hyland 44-36 and Enneberg 22-6). Figure 2.2-1 shows the location of these wells, along with other Duperow wells without geophysical logs, in the UTM coordinate system. Also shown in this figure are the 3D seismic survey area (pink outline), the production region (dark gray outline), and the injection region (red outline).
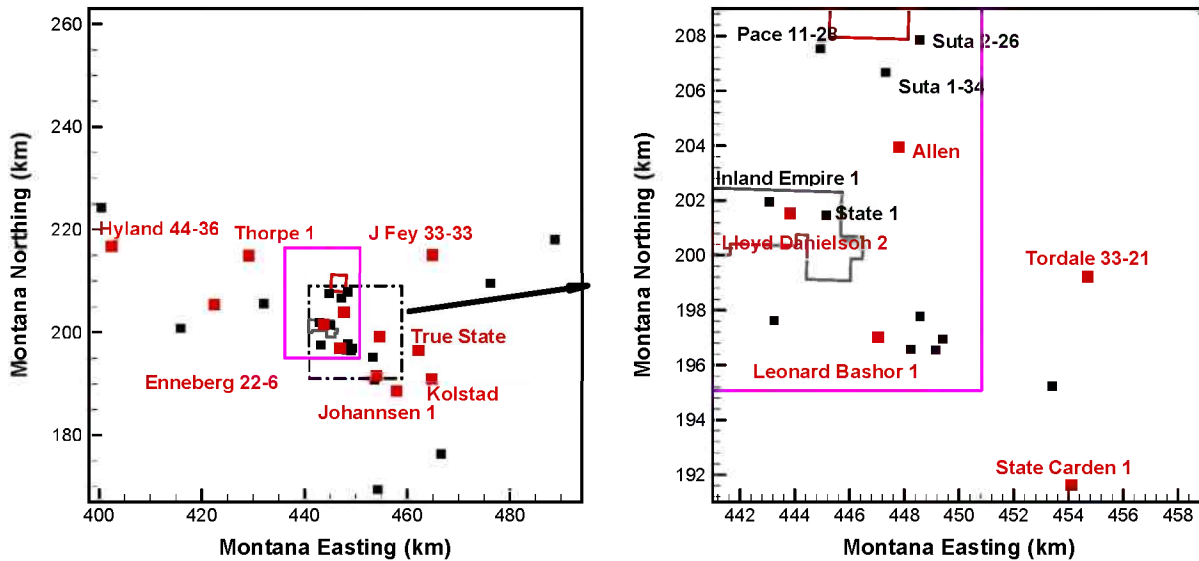
Figure 2.2-1. *Location of wells (in black symbols) and wells with good geophysical logs (in red symbols) near the project 3D seismic survey area (in pink polygon), the production region (in gray) and the injection region (in red). Also given are the names of the wells with geophysical logs for reference.*

Figure 2.2-2 shows the gamma ray, calculated intrinsic permeability, and neutron, total, and effective porosity logs for the 12 wells. As the top panel shows, a high-porosity zone exists in the middle Duperow for all four wells, and it is this zone that will be targeted for CO_2 injection. The porosity of this zone ranges from 4% to 20%, with an average of 8%. For the six nearby wells, the porosity zone varies significantly in terms of its thickness and even its presence. For the two western wells, there is no clear high-porosity zone. Also note that many of these logs were obtained in the 1950s or 1960s, and their quality may not be very high. When the new logs are available from the production, injection, and monitoring wells, comparisons will be made with these old logs.
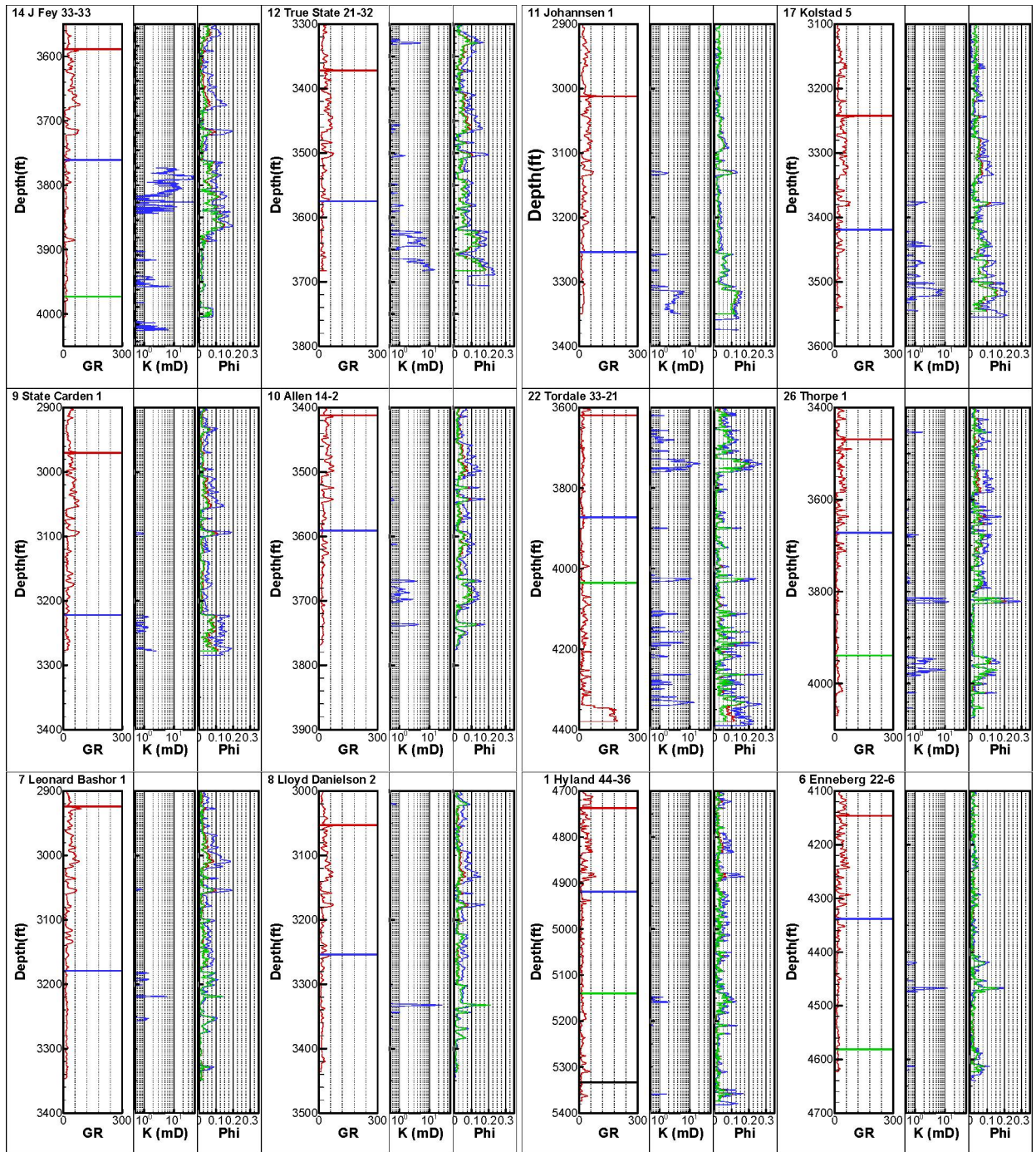
Figure 2.2-2. *Logs of gamma ray, calculated intrinsic permeability, and neutron, total, and effective porosity of the 12 wells located near the project site. The top elevations of upper, middle, and lower Duperow are marked with red, blue, and green separators, respectively.*

2.2.2. Geochemical Data

Geochemical data from the literature and from available public sources of information were reviewed, to establish a representative sediment mineralogy and brine composition to use in geochemical and reactive transport modeling investigations (Section 5). This geochemical characterization effort focused on the Duperow formation (of Devonian age), which is the target formation for injection.

2.2.2.1. Mineralogy

The mineralogy used for geochemical and reactive transport modeling, shown in Table 2.2-1, was based on descriptions of the Duperow formation by Wilson (1967) and recent petrographic work by Ryerson et al. (2013). The amounts of the main minerals calcite, dolomite, ankerite, and anhydrite were calculated to yield whole-rock elemental compositions in the range of those reported by Ryerson et al. (2013). Wilson (1967) reports that in the Duperow limestone rock types, insoluble residue is always less than 2 wt %, consisting of pyrite, illite, mica, and quartz. Ryerson et al. (2013) provide similar information, reporting less than 3 wt % of silicate minerals in analyzed samples, with quartz being the most common. These authors also report trace minerals pyrite, fluorite, and sometimes (in anhydrite-rich layers) celestite, as well as K-feldspar inclusions in dolomite and anhydrite. These minerals were included in the simulations as primary minerals, except for celestite ($SrSO_4$), the presence of which in the model resulted in dissolved Sr concentrations that seemed untypically elevated. Traces of strontianite ($SrCO_3$) were considered in place of celestite, yielding lower Sr dissolved concentrations. Illite/mica phases were modeled using muscovite as a proxy mineral (Section 5.2).

Table 2.2-1. Mineralogy of the Duperow formation assumed for modeling investigations (amounts are on a dry solid basis)

Minerals	Weight %	Volume %
Calcite	69.7	71.3
Dolomite	20	19.4
Ankerite	3	2.5
Anhydrite	4	3.7
Quartz	2	2.1
Pyrite	0.6	0.33
Strontianite	0.05	0.03
K-spar	0.3	0.33
Fluorite	0.01	0.01
Illite/mica	0.3	0.30

2.2.2.2. Brine Composition

The brine composition for the modeling effort was reconstructed on the basis of data available from the US Geological Survey (USGS) database of produced waters, together with geochemical modeling (Section 5.2). The NATCARB brine database was also consulted, but was found to contain essentially the same data as those in the USGS database for our area of interest.

The USGS database was filtered to retrieve all samples in Montana from formations labeled either as Devonian, or specifically labeled as from the Duperow formation, and from either the

Sweetgrass Arch or Williston Basin geologic provinces. The filtered data were reviewed and analyzed using elemental correlation plots, Schoeller, Stiff, and Piper diagrams. The samples closest to the site, shown in Table 2.2-2, were compared to the entire collected dataset, to determine whether these samples exhibit compositional trends similar to those observed for the bulk of the filtered data.

Table 2.2-2. General information for brine samples filtered from the USGS produced water database for locations closest to the site. "Plot ID" letters were assigned in this report to simplify reference in the text and figures. Distances from the site were approximated from geographic coordinates given in the database.

Plot ID	UNIQID	COUNTY	GEOBASIN	WELLNAME	SAMPFORM	TOP (ft)	BOT (ft)	TDS (mg/L)	Appox. distance from site
B	25000655	TETON	SWEETGRASS ARCH	STATE OF MONTANA D-1	DEVONIAN	3300	3370	9508	90 mi South
C	25000763	TOOLE	SWEETGRASS ARCH	#1 MCKECHINE	DEVONIAN	3620	3659	218595 (ppm)	35 mi South
C	25000764	TOOLE	SWEETGRASS ARCH	#1 MCKECHINE	DEVONIAN	3560	3568	216329	35 mi South
D	25001328	PHILLIPS	WILLISTON BASIN	1 LOUIS TUMA	DUPEROW	4898	4937	47405	200 mi West
D	25001329	PHILLIPS	WILLISTON BASIN	NO. 1 LOUIS TUMA	DUPEROW	4898	4937	46094	200 mi West
E	25002191	CASCADE	SWEETGRASS ARCH	1 BLOOM	DUPEROW DEVONIAN	4728	4895	10681	100 mi South

Samples from the closest well to the site (C, Table 2.2-2) are labeled as being from Devonian formations within the Sweetgrass Arch geologic province, but not specifically from the Duperow formation. The composition and high salinity (219,000 ppm) versus shallow depth of these brine samples appear off the trend of other data specifically labeled as being from the Duperow formation, but from locations farther away in the Williston Basin (Figure 2.2-3). Two other data points within the Sweetgrass Arch province (B and E) display low salinities and quite different water chemistries from the other samples (Figures 2.2-3 and 2.2-4). Points D appear to be more in line with other data from the Duperow formation, in terms of salinity-depth relationship and proportions of dissolved constituents. For these reasons, the composition of these samples was used as a starting point for the reconstruction of *in situ* brine composition (Section 5.2). For all brine samples considered, elemental correlation plots were also drawn to further examine compositional ranges and relationships with respect to seawater evaporation or dilution trends (Figure 2.2-5). For most samples, Na/Cl ratios closely follow that of seawater. For high salinity samples, calcium concentrations become quite enriched relative to seawater, which likely reflects dolomitization and albitization processes. The inverse relationship between sulfate and calcium (Figure 2.2-5) in concentrated brines also suggest anhydrite as one of the controlling phases for the solubility of these elements.
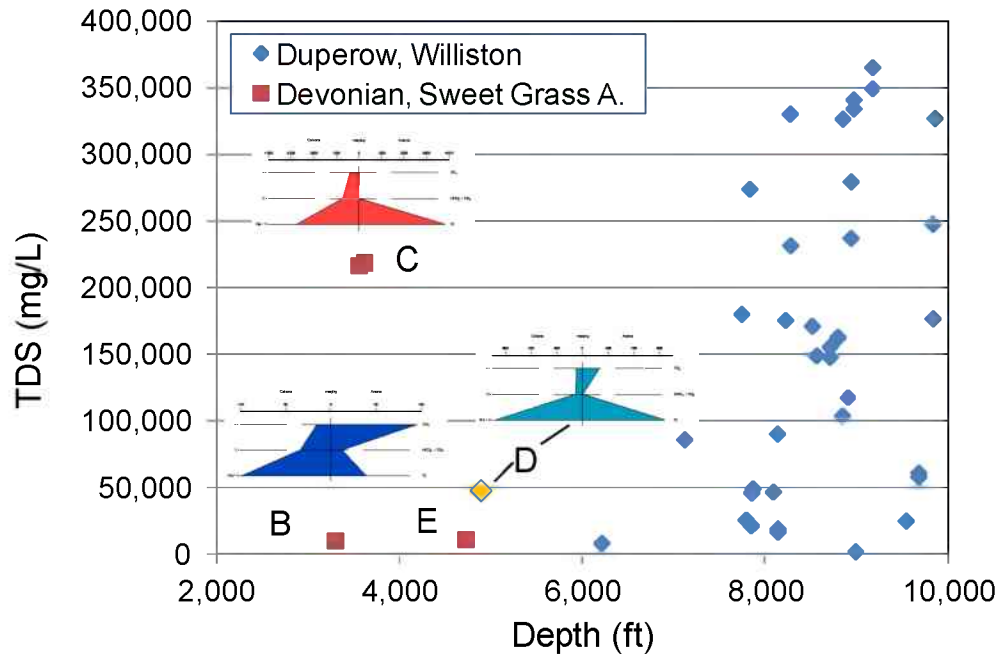
Figure 2.2-3. *Salinity versus depth graph for samples from the USGS produced water database, showing data points B, C, D, E in Table 2.2-2 as well as other data points for samples labeled as from the Devonian and/or the Duperow formation in Montana. Superposed Stiff diagrams on data points show variations in the chemical types of these waters (relative proportions, from top to bottom of each diagram: left-hand side Mg, Ca, Na+K; right-hand side SO_4, (H)CO_3, Cl).*
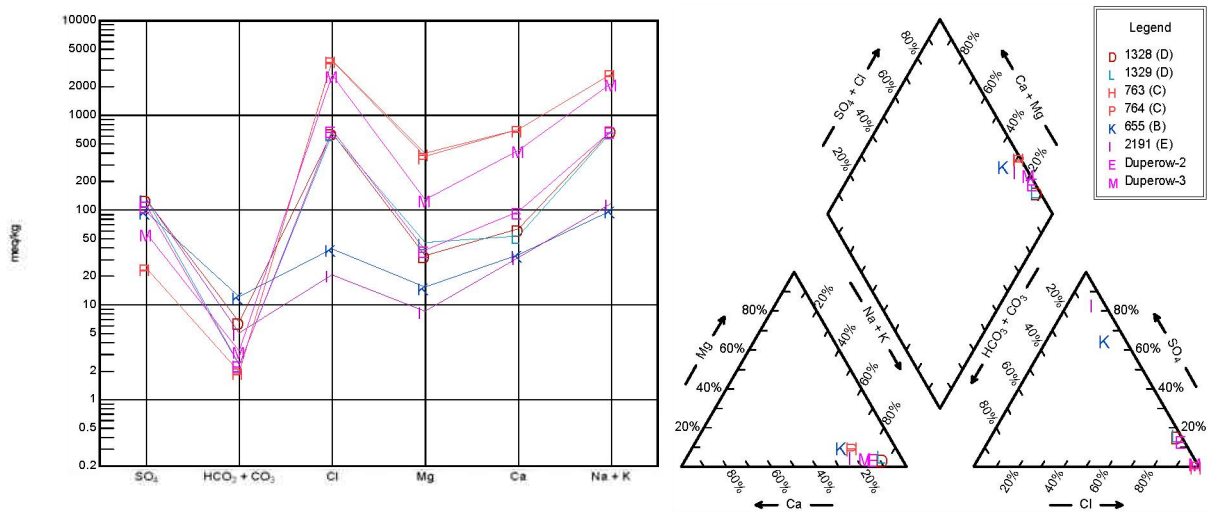
Figure 2.2-4. *Schoeller (left) and Piper diagrams for brine samples identified in Table 2.2-2. Points Duperow-2 and Duperow-3 are reconstructed compositions, with Duperow-2 used for geochemical modeling analyses in this report (Section 5.2).*
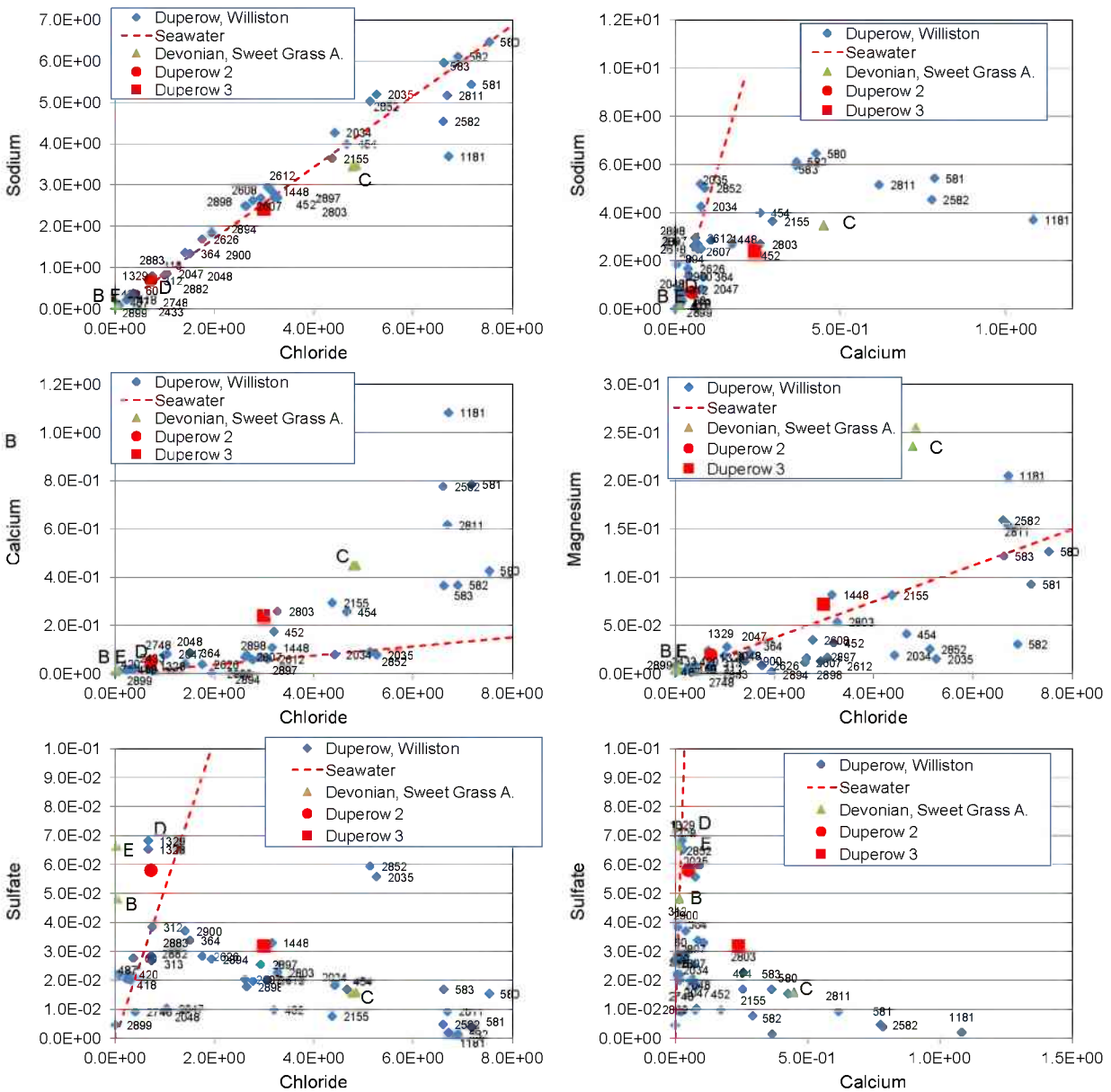
Figure 2.2-5. *Comparison of data from the USGS produced waters database in Montana (for samples from locations as labeled in the legend). Letters correspond to plot ID in Table 2.2-2, and numbers to truncated USGS ID numbers. Points Duperow 2 and Duperow 3 are reconstructed compositions, with Duperow 2 used for modeling analyses in this report (Section 5.2). The dashed line represents the seawater evaporation/dilution trend.*

2.3. Static Geologic Model

The development of a 3D geologic (static) model for Kevin Dome was initiated by Schlumberger, using well data and constrained by 2D seismic survey data (Brown, 2012). This initial geologic model focused on the production and injection areas. Later, it was updated and expanded to include the entire dome structure, by including data from additional wells (Will, 2013). LBNL contributed to the decision about the extent of the updated geologic model, which ended up covering the entire structure of Kevin Dome. Here, we briefly describe the main

features of the geologic model that are relevant to the LBNL multiphase flow modeling effort (Sections 3 and 4). For the details of the static geologic model developed by Schlumberger, the reader is referred to Will (2013). Figure 2.3-1 shows the geologic model domain (thick black line), the 3D seismic survey region (pink line), the CO_2 injection region (red line), and the production region (gray line), as well as the locations of wells (black symbols) and wells with geophysical logs (red symbols). This geologic model covers a region of 125 km × 86 km, with 11 townships in the easting and 8 townships in the northing directions.
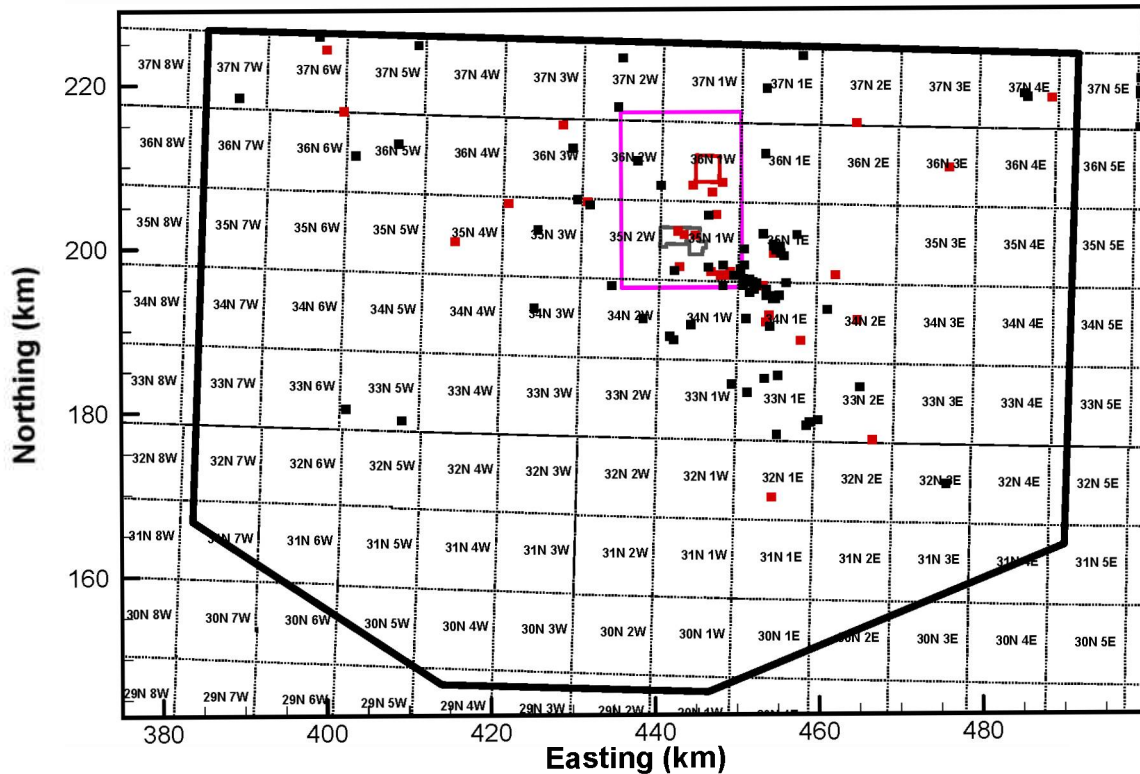
Figure 2.3-1. *The domain of the 3D geologic model (in thick black polygon), wells with (in red squares) and without (in black squares) geophysical logs, respectively, that were used for constructing the 3D geologic model, the seismic survey region (in pink), the production region (in gray), and the injection region (in red)*

In the vertical direction, the 3D geologic model covers the Banff, Bakken, Three Forks, Potlach, Nisku, Duperow, Souris River, and Cambrian formations. These formations are immediately underlying the Madison formation, which is considered the lowermost USDW (see Section 6). The Duperow formation was further divided into the upper, middle, intermediate, and lower units. In the geologic model, only one model layer is used for each formation, except the Nisku formation (which consists of 10 model layers) and the Duperow formation. The four units of the Duperow formation consist of 30, 30, 20, and 30 model layers, respectively (Will, 2013). The geologic model not only provides the top elevation and thickness of each model layer, and thus formation or unit, but also provides the porosity and permeability fields generated using algorithms built in to the Petrel software. At this stage of the Kevin Dome project, all the porosity and permeability fields are extremely uncertain, because no permeability data are available, and porosity data are only available from geophysical logs at 30 wells.

Figure 2.3-2 shows the thickness of the Banff, Bakken, and Nisku formations, and the upper, middle, and lower Duperow units within the 125 km × 86 km area, while Figure 2.3-3 shows the top elevation of these formation or units. These two figures show the details of the top elevation and thickness of these formations or units in the vicinity of the injection region and the production region.
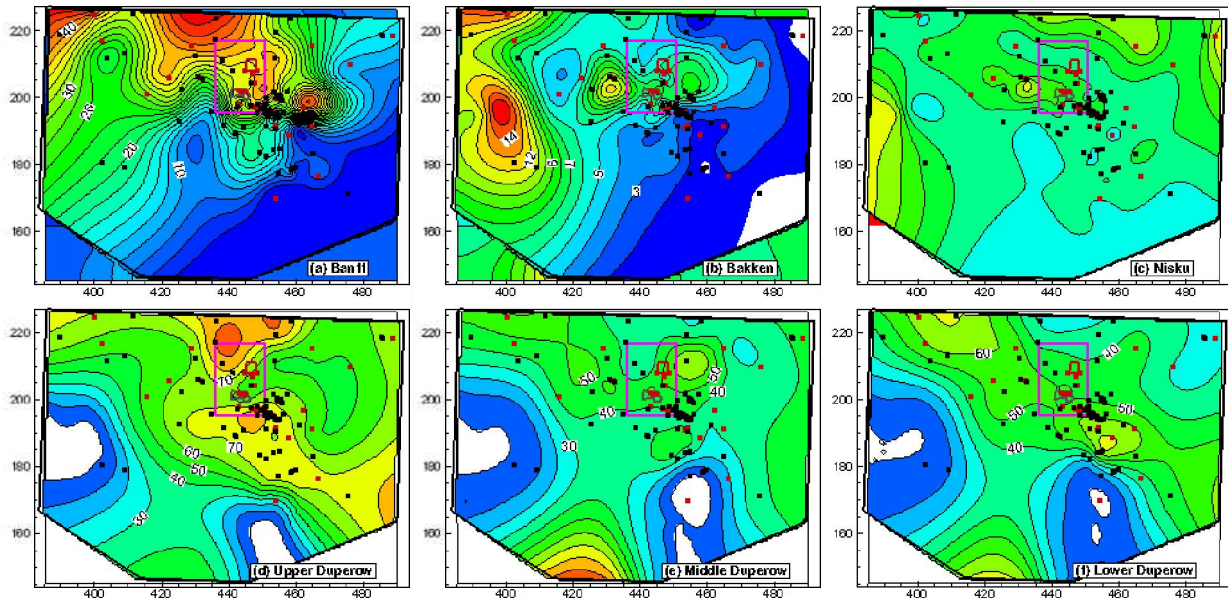
Figure 2.3-2. *Contours of formation thickness of the Banff formation, the Bakken formation, the Nisku formation, and the upper, middle, and lower Duperow units, with wells without (in black squares) and with (in red squares) geophysical logging used for constructing the 3D geologic model, the seismic survey region (in pink), the production region (in gray), the injection region (in red), and the model boundary (thick black polygon)*
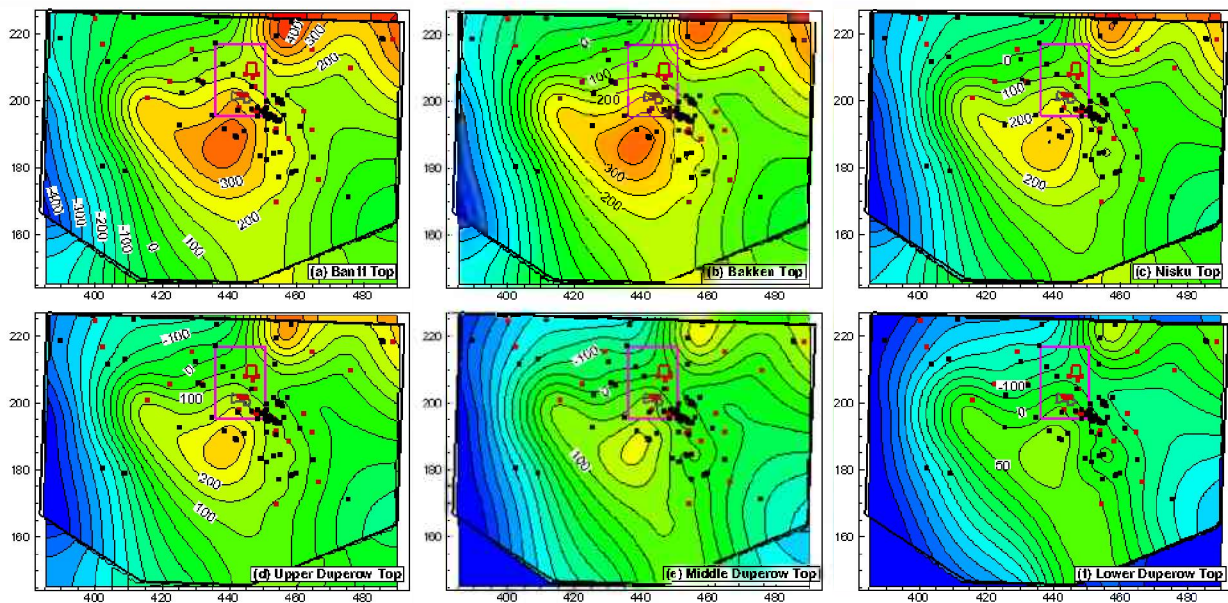
Figure 2.3-3. *Contours of the top elevation (relative to the subsea level) of the Banff formation, the Bakken formation, the Nisku formation, and the upper, middle, and lower Duperow units.*

Figure 2.3-4 shows the top elevation and thickness of the middle Duperow unit within a 35 km × 35 km region near the CO_2 injection and production regions. The top elevation varies from -200 m to 200 m TVDss (Total Vertical Depth subsea), and the injection region (in red polygon) is located at the saddle between the dome structure of Kevin Dome in the southwest direction and the Sweetgrass Hills in the northeast direction. The top elevation of the injection region is approximately at 0 m. The injected CO_2 may migrate, under buoyancy, to the dome structure, to the Sweetgrass Hills, or to the southeast direction, based on the top elevation of the middle Duperow in the vicinity of the injection region. The thickness of the middle Duperow is ~50 m in the injection region, while it varies from 30 m to 60 m within the 35 km × 35 km region near the injection and production regions.
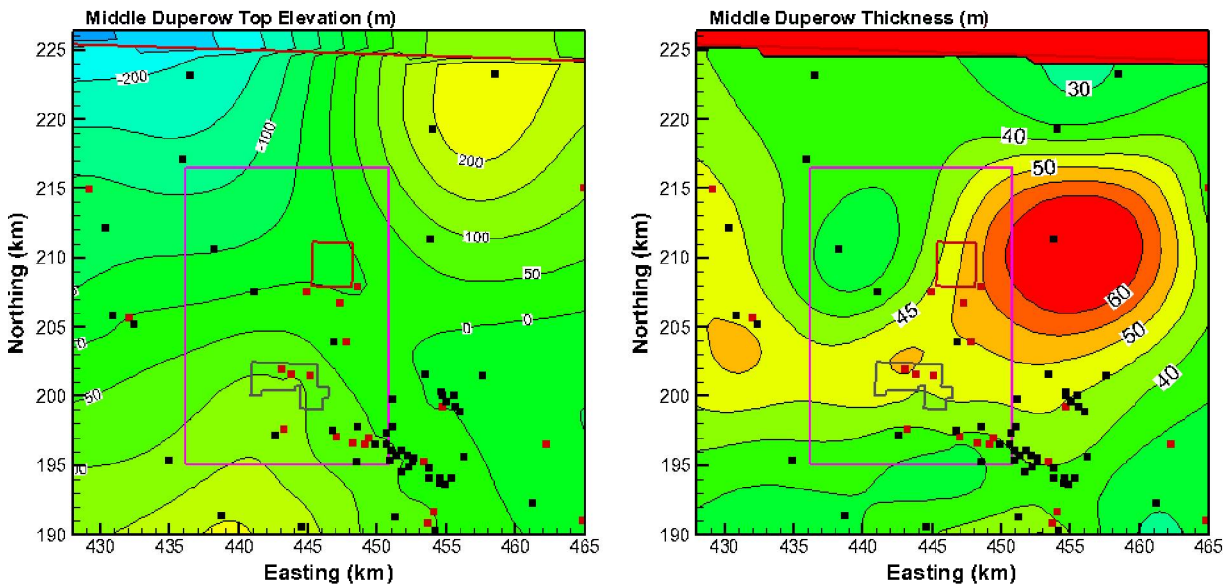
Figure 2.3-4. *Contours of the top elevation and thickness of the middle Duperow in the vicinity of production and injection areas. Refer to Figure 2.3-2 for the meanings of symbols and lines.*

3. MULTIPHASE FLOW MODELING FOR CO_2 INJECTION

A three-dimensional (3D) model was developed to simulate two-phase CO_2-brine flow in response to CO_2 injection into the middle Duperow at Kevin Dome. The goal of the simulations was to answer key questions about injectivity, pressure rise, plume size, storage efficiency, and long-term plume migration, and Area of Review (AoR), among others. The design injection rate is 7.92 kg/s, equivalent to 1 million tonnes (1 tonne = 1.1 ton) CO_2 in four years. The base case consisted of a step-rate injection scheme with assumed permeability of 30 md and a porosity of 0.08 in the middle Duperow. To address uncertainty in rock properties, different cases were simulated with varying permeability and porosity, as well as different step-rate injection schedules.

3.1. 3D Model Development

3.1.1. Determination of Model Domain

The model domain was determined so that the boundary effects on the pressure buildup and CO_2 plume are negligible during the 4-year injection period and the 2-year post-injection period. This model domain is 50 km × 40 km, which is cut from the larger 3D geologic model (see Section 2.3), and is approximately centered at the injection well at (24791.7 m, 23508.3 m) in the shifted coordinates, with the northern boundary at the U.S.-Canada border and all other lateral boundaries as shown in Figure 3.1-1.
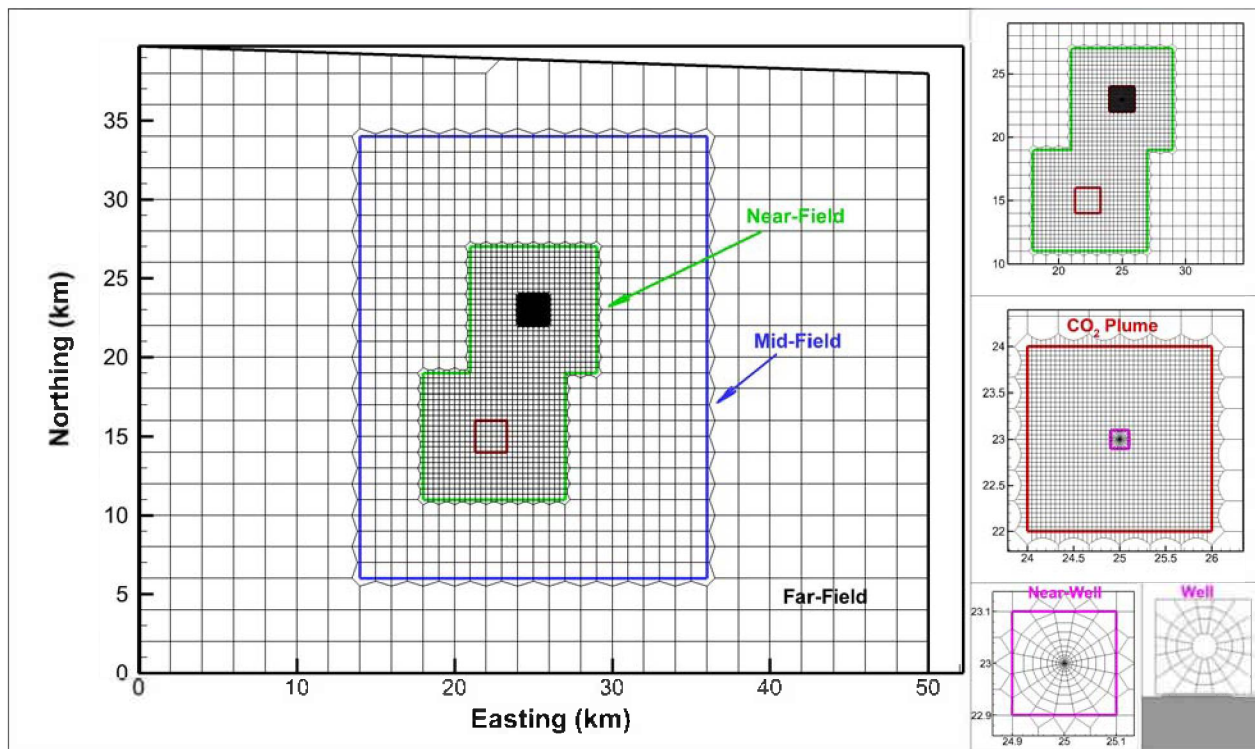
Figure 3.1-1. *2D Model domain with the far-field, mid-field, near-field, CO_2 plume, and near-wellbore regions, and 2D mesh with varying gridblock resolutions in the different regions*

In the vertical direction, we limited the 3D model to the following formations or hydrogeologic units: the Nisku formation and the upper Duperow unit as cap rock, the middle Duperow unit as the storage formation, and the intermediate Duperow unit, the lower Duperow unit and the Souris River formation as the basement rock. The determined 3D numerical model domain is a subset of the larger 3D geologic model domain in both the horizontal and vertical directions.

3.1.2. 2D and 3D Mesh Generation

We designed the map-view mesh (2D mesh) by roughly defining the far-field, mid-field, near-field, CO_2 plume, and near-wellbore regions. For example, to accurately simulate CO_2 migration and trapping, we used a 3.5 km $\times$ 3.5 km area to define the CO_2 plume region centered at the injection well, excluding the near-wellbore region defined as 200 m $\times$ 200 m around the well (see Figure 3.1-1). To simulate the fast-propagating pressure buildup, we used a near-field region of 11 km $\times$ 16 km (excluding all the inner regions: the plume region and the near-wellbore region), a mid-field region of 22 km $\times$ 28 km, and a far-field region for the entire area outside of the mid-field region.

The gridblock size in the far-field, mid-field, near-field, and the plume region is 2 km $\times$ 2 km, 1 km $\times$ 1 km, 1/3 km $\times$ 1/3 km, and 50 m $\times$ 50 m, respectively, and the submesh within each region is uniform. To accurately simulate the bottom-hole pressure at the injection well, a radial local mesh was developed within 100 m around the injection well, with the radial discretization varying from 20 m to 0.07 m at the wellbore gridblock (see Figure 3-1.1). A cement-casing layer of 0.2 m thick was included for future investigations (not reported here) into whether perforation properties could affect the bottomhole pressure significantly. This special mesh design with local mesh refinement leads to a total of 4448 2D (map-view) cells.

In the vertical direction, 40 model layers were used, including 1 layer for the Nisku formation, 5 layers for the upper Duperow unit, 25 layers for the middle Duperow unit, 3 layers for the intermediate Duperow unit, 4 layers for the lower Duperow unit, and 2 layers for the Souris River formation. Figure 3-1.2 shows the generated 3D mesh with a total of 177,920 3D gridblocks and 551,768 connections.
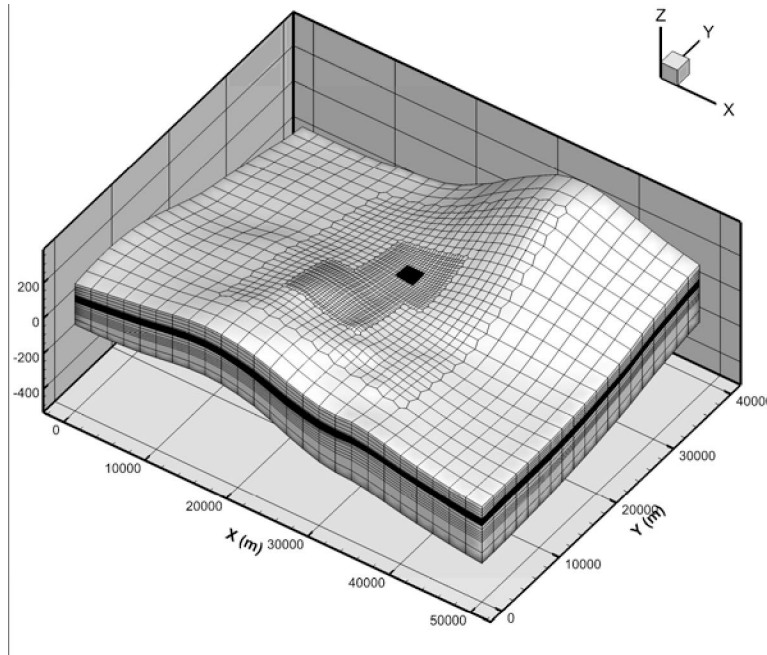
Figure 3.1-2. Generated 3D mesh with 30 times vertical exaggeration. Note that the vertical axis is the true elevation relative to sea level.

3.1.3.   Initial and Boundary Conditions

Based on the pressure measurements at several wells in the middle Duperow in the injection region, MSU estimated that the average hydraulic gradient in the middle Duperow (from the water table) is 0.35 psi/ft or 0.8 m/m (Fairweather, personal communication) (see Figure 6.2-2), indicating ~20% underpressure relative to a hydrostatic gradient that is typically ~0.433 psi/ft (0.98 m/m). A hydrostatic pressure was calculated based on the water density and the depth to the top of the middle Duperow at the injection well, and a pressure of 20 bar (2 MPa) below hydrostatic value (~100 bars or 10 MPa) was fixed at the top middle Duperow gridblock at the injection well to account for the underpressure. A simulation was conducted to obtain the equilibrated pressure conditions in the domain, with the initial conditions for salt mass fraction and temperature of 0.13 and 34.4°C, respectively. As a result, the entire 3D model domain (including the cap rock and basement rock) is underpressured approximately consistent with the expected 0.35 psi/ft (0.8 m/m) hydrostatic gradient. The final results after 1000 years from the equilibrium simulation run were used as the initial conditions for the CO_2 injection simulation. Note that a uniform salt mass fraction and temperature are used.

In all of the following simulations, no-flow conditions were used for all lateral boundaries as they are far away from pressure perturbations, and fixed pressure conditions were used at the top and bottom boundaries. At the injection well, the middle Duperow is 50 m thick (see Figure 2.3-4) and the geophysical logs for some nearby wells show that the high-porosity middle Duperow is ~30 m thick. The top 30 m zone (15 model layers) was used to represent the perforated zone in the well for CO_2 injection. A variable injection rate was used to maximize injectivity while minimizing pressure rise. The design injection rate is 7.92 kg/s, i.e., injecting 1 million tonnes in four years.

3.1.4.　　Simulations

All simulation runs were conducted using TOUGH2-MP (Zhang et al., 2008), the parallel version of TOUGH2 (Pruess et al., 1999, 2011), with the equation-of-state module ECO2N (Pruess, 2005) on an LBNL cluster computer.

To avoid hydraulic fracturing of the storage formation and cap rock, we compared simulated pressure buildup (ΔP) to the critical pressure buildup (ΔP_f), which could induce fracturing. It was assumed that the fracturing gradient is 170% of the hydrostatic pressure. Considering the depth of the middle Duperow (~1000 m), the critical pressure increase is 70 bar. As a result, ΔP_f = 70 bar + 20 bar (underpressure) = 90 bar was used as the critical fracturing pressure in this study.

3.2.　　Modeling Results: Base Case

As shown in Section 2.2.1, porosity is available only from geophysical logs from 30 wells near the project site. There are no core data for porosity and permeability. The permeability calculated from the log data on porosity is highly uncertain (Brown, 2012). As a result, the base-case modeling presented here is based on assumed rock porosity and permeability. As soon as site-specific or representative data become available, we will update the model and rerun the simulations.

3.2.1.　Rock Properties in the Base Case

In the base case, a permeability of 30 md and a porosity of 0.08 were used for the high-porosity zone (~30 m thick) of the middle Duperow, and a permeability of 0.25 md and a porosity of 0.05 were used for the low-porosity zone of the middle Duperow. The capillary pressure was simulated using the van Genuchten (1980) model with capillary entry pressure of 0.125 bar and parameter m equal to 0.457. The water relative permeability of the van Genuchten-Mualem model (1980) was used with parameter m = 0.457 and residual water and gas saturation of 0.5 and 0.25, respectively. The Corey (1954) model was used for gas relative permeability. The upper, intermediate, and lower Duperow were assumed to have a porosity of 0.05 and a permeability of 0.01 mD, while the Nisku and Souris River have a porosity of 0.05 and a permeability of 0.0001 md. The pore compressibility for all formations was assumed to be 1.628 $\times$ 10^{-9} Pa^{-1} (Fatt, 1958).

3.2.2.　Results for Pressure Buildup

Figure 3.2-1 shows the spatial distribution of pressure buildup at the top model layer of the middle Duperow at 1, 2, and 4 years during the injection period, and 6 years (2 years after injection shut-in) during the post-injection period. At 1 year of injection, pressure buildup appears to be quasi-radial, with a radius of ~5 km for ΔP > 0.1 bar. As shown in the insert, ΔP is higher than 90 bar within a radius of 220 m, indicating possible hydrofracturing near the wellbore. Along the radius direction, ΔP decreases quickly to 0.1 bar at a radius of 5 km, because of low permeability in the middle Duperow, and two-phase conditions near the injection well.
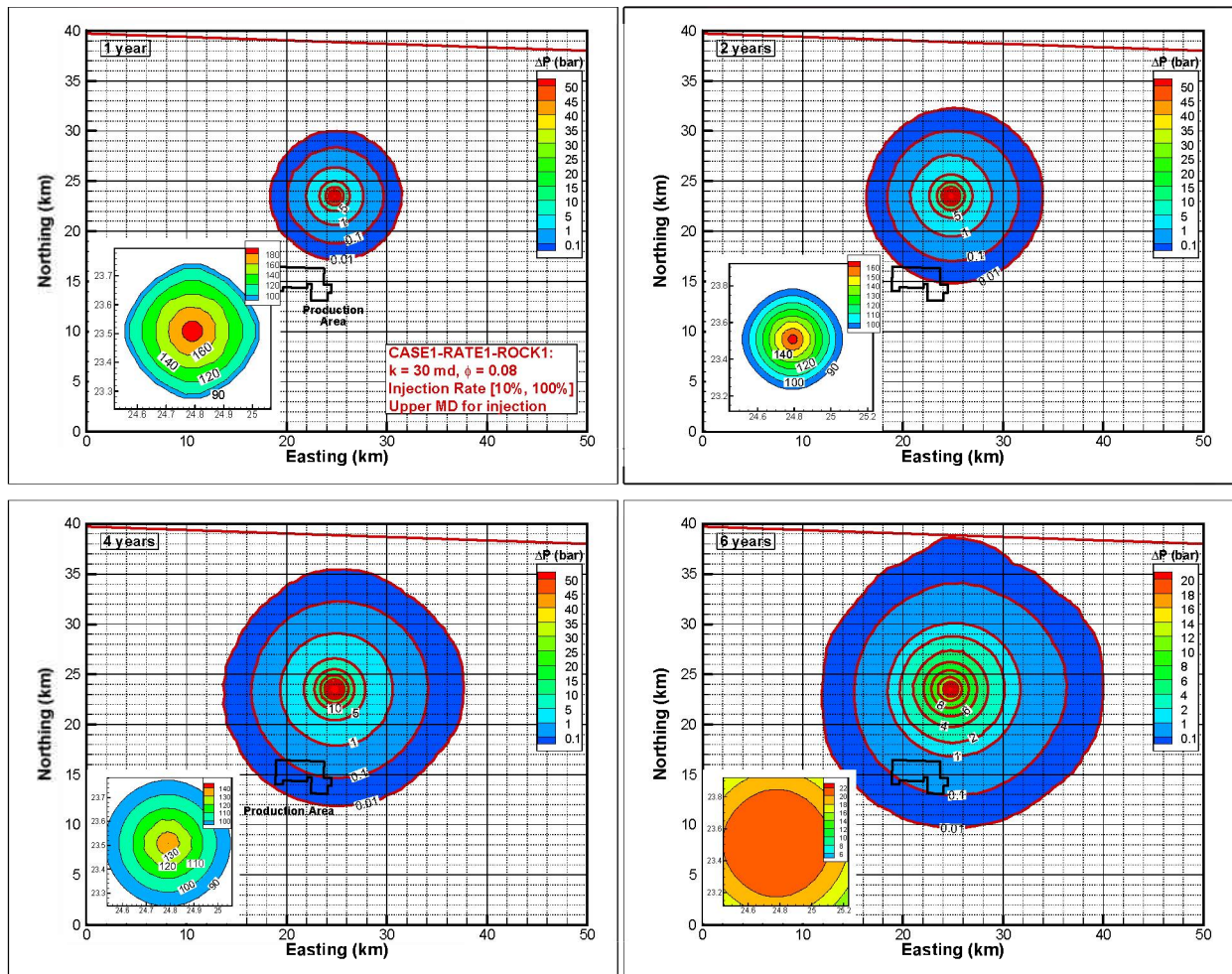
Figure 3.2-1. *Simulated pressure buildup (in bar) at 1, 2, and 4 years during the injection period, and 6 years during the post-injection period, all from the start of CO_2 injection for the base case of injection schedule and rock properties. The inserts show high pressure buildup near the injection well which should be compared with the critical fracturing pressure increase of 90 bar.*

With time, the radius of the pressure front becomes larger and larger. At four years, the 0.1 bar pressure front has a radius of ~10 km from the injection well, but has still not reached the U.S.-Canada border. The highest ΔP near the injection well decreases with time, but the size of the region with $\Delta P \geq 90$ bar becomes larger, with a radius of 250 m. Note that ΔP in the production region is relatively small, less than 0.3 bar, indicating injection may have little impact on CO_2 production.

After 2 years of injection shut-in, the ΔP front of 0.1 bar continues to expand, but is still short of the U.S.-Canada border. Indeed, ΔP is about 0.01 bar at the point on the border nearest to the injection well. This indicates that the effect of lateral boundaries on pressure buildup is negligible. Near the injection well, ΔP increases dramatically, with maximum ΔP of 22 bar.

3.2.3. Results for CO_2 Saturation

As shown in Figure 3.3-2, the CO_2 plume increases in size with time. The majority of the plume has a saturation between 0.3 and 0.4, a result of the large residual water saturation (0.5) used in

the study. The residual water saturation is based on the results of many laboratory experiments on core samples of a variety of sandstones. At the end of injection, the plume has a radius of 750 m.

Figure 3.2-2. *Contours of simulated CO_2 saturation in the top model layer of the middle Duperow at 1, 2, and 4 years during the injection period, and 6 years during the post-injection period, all from the start of CO_2 injection for the base case injection schedule and rock properties.*

Note that the quasi-radial CO_2 plume is a result of assumed homogeneity of rock properties, since the spatially varying thickness and slope of the middle Duperow is relatively small near the injection well. When heterogeneity (unknown) is considered, the effective porosity for CO_2 migration will be much smaller. This fact has been observed at all existing storage test and pilot

injection sites. In short, the actual plume size is expected to be significantly larger than the homogeneous base-case simulation suggests.
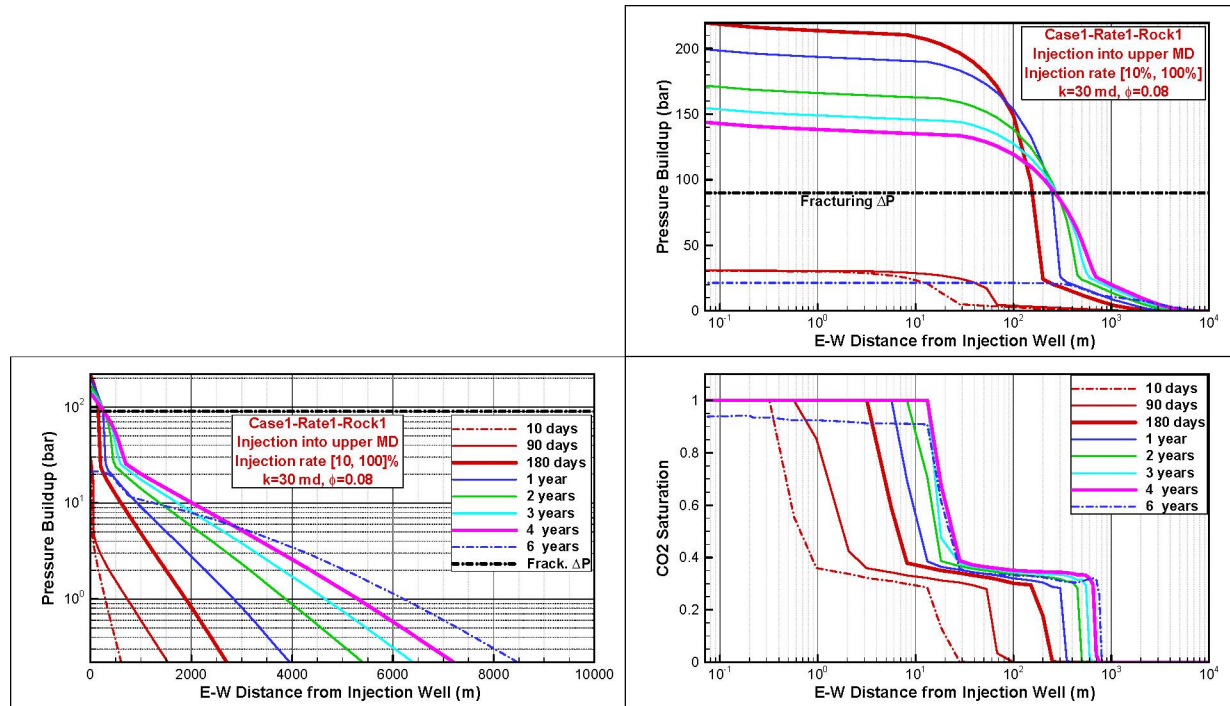
Figure 3.2-3. *The east-west profiles of pressure buildup and CO_2 saturation at the injection well as a function of time showing the region of very high ΔP near the injection well.*

Figure 3.2-3 clearly shows the distribution of ΔP and CO_2 saturation (S_{CO2}) and their relationship in the east-west direction at the injection well. The ΔP distribution is very different in three regions of S_{CO2}: the near-wellbore dry-out zone, the dominant two-phase flow zone, and the single-phase brine flow zone. These three zones are separated from each other by two sharp fronts. The first front is between $S_{CO2} = 1$ and $S_{CO2} = 0.38$, with a linear drop with $\log(R)$; while the second front is between $S_{CO2} = 0.30$ and $S_{CO2} = 0.0$, with an even sharper drop, a feature of self-sharpening of two-phase flow. As shown in the S_{CO2}-$\log(R)$ plot, the size of the CO_2 plume increases with injection time. Out of the CO_2 plume, $\log(\Delta P)$ almost linearly changes with radial distance (see right panel $\log(\Delta P)$-R plot), while ΔP is close to 25 bar at the front of the CO_2 plume after 180 days.

As shown in the ΔP-$\log(R)$ plot, ΔP does not change significantly within the dryout zone, because the viscosity of CO_2 is much smaller than that of brine, and CO_2 relative permeability is 1.0. The ΔP change is also small within the first front. The dramatic change in ΔP with $\log(R)$ occurs within the two-phase flow zone, where CO_2 relative permeability is relatively small. For example, at 180 days, the two-phase zone is located between $R = 13.1$ m and 200 m, and ΔP drops from 210.5 bar to 24.3 bar. All of these indicate that it is CO_2 relative permeability that produces a large ΔP, which is higher than ΔP_f in the vicinity of the injection well. Note that there is a large uncertainty in CO_2 relative permeability in the preliminary modeling. A site-specific function for relative permeability is critical to accurate simulation of pressure buildup.

3.3. Modeling Results: Sensitivity Analysis

Manual sensitivity analysis was conducted for permeability and porosity in the assumed homogeneous middle Duperow. Further sensitivity analysis was conducted by a gradual increase in CO_2 injection rate to enhance CO_2 injectivity.

3.3.1. Effect of Permeability and Porosity

Case ROCK2 had a permeability of 80 md and a porosity of 0.08, while case ROCK3 had a permeability of 80 md and a porosity of 0.15. The injection scheme (RATE1) was used. Figure 3.3-1 shows the ΔP distribution at 1, 2, 4, and 6 years of injection for both cases. In case ROCK2, the ΔP front is larger in comparison to the base case, and ΔP near the injection well is less than the critical pressure increase ΔP_f. The $\Delta P = 0.01$ bar front reaches the U.S.-Canada border before 4 years. At 6 years, the border experiences a ΔP of 0.03 bar, but the front of $\Delta P = 0.1$ bar does not reach the border. The pressure front does not reach any other lateral boundaries. In comparison to case ROCK2, ΔP in case ROCK3 has a smaller ΔP front over the entire simulation period, because the hydraulic diffusivity in case ROCK3 is smaller than that in case ROCK2. It is hydraulic diffusivity that controls the ΔP front propagation in the single-phase flow region.

We compared the CO_2 plume size in all three cases, and found both permeability and porosity affect the CO_2 plume size. Table 3.3-1 shows the time-dependent radius of the CO_2 plume in the three cases. With an increase in permeability, the plume size at the top of the middle Duperow increases. For example, at $t = 4$ years, the plume radius is 800 m and 950 m in cases ROCK1 and ROCK2 respectively. However, the increase in porosity leads to a smaller plume radius. For example, the plume radius reduces from 950 m (ROCK2) to 700 m (ROCK3) when porosity increases from 0.08 to 0.15, while all other parameters are kept unchanged. Figure 3.3-2 shows the contours of CO_2 saturation for the entire plume at 1, 2, 4, and 10 years in both cases (ROCK2 and ROCK3).

Table 3.3-1. Time-dependent radius of the CO_2 plume in the three different cases

	180 days	1 year	2 years	4 years	6 years	10 years
ROCK1	300 m	400 m	550 m	800 m	850 m	900 m
ROCK2	300 m	400 m	650 m	950 m	1000 m	1050 m
ROCK3	250 m	350 m	500 m	700 m	750 m	800 m

Note the relationship between pressure and CO_2 saturation responses to the different rock properties (see Figure 3.3-3). As shown, ΔP is always higher in case ROCK3 than in case ROCK2 when porosity is increased from 0.08 to 0.15. Meanwhile, the radii of the three regions of CO_2 dryout zone, two-phase flow zone, and single-phase brine-flow zone decrease with increased porosity. This is understandable, because a unit volume of porous medium can store more CO_2 because of a larger porosity. Because of the two-phase zone with a smaller radius and relatively small CO_2 relative permeability, ΔP is relatively higher in case ROCK3. This leads to a ΔP higher than ΔP_f over a shorter time period, around 180 days.
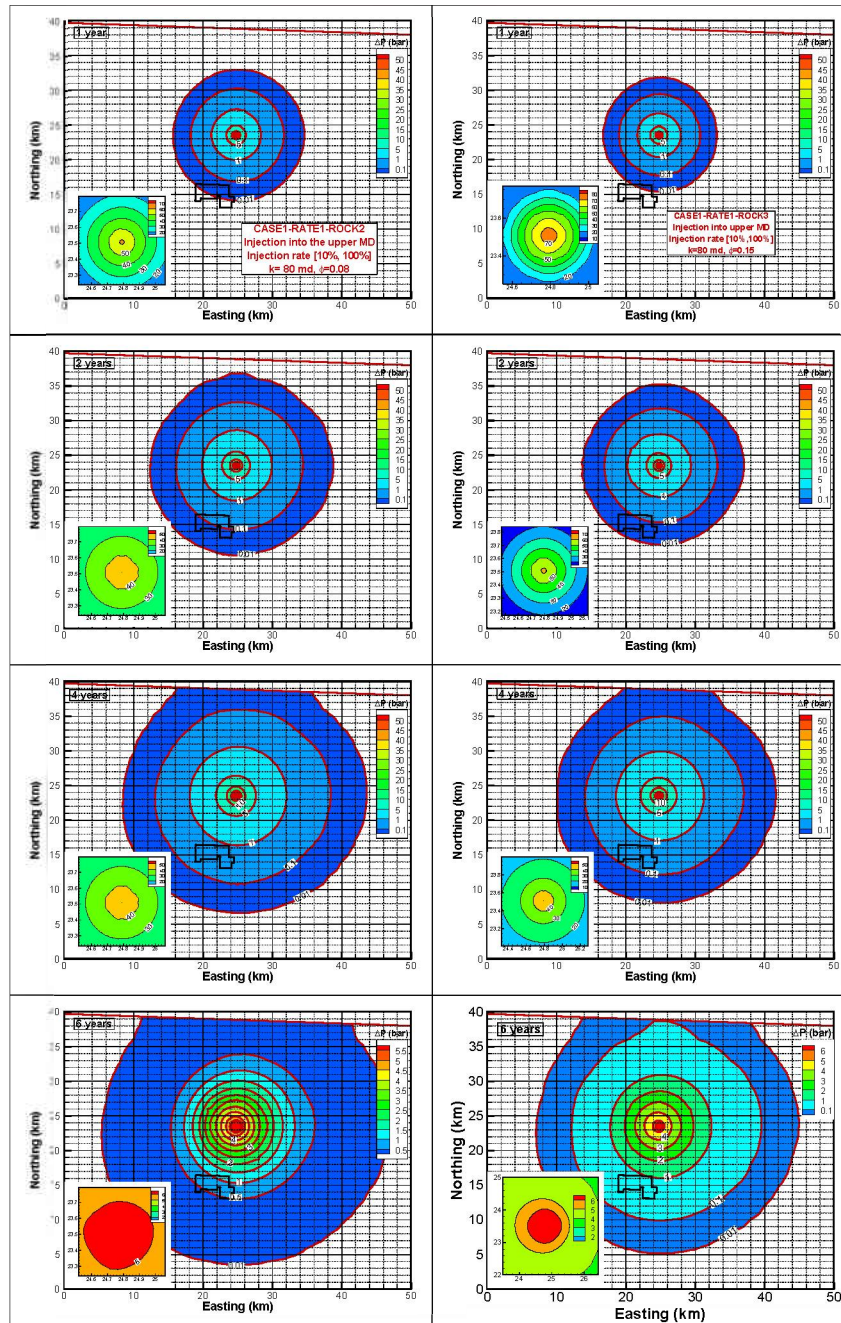
Figure 3.3-1. *Contours of simulated pressure buildup (in bar) at 1, 2, and 4 years during the injection period, and 6 years during the post-injection period in cases ROCK2 and ROCK3. The inserts show high pressure buildup near the injection well to compare with the defined fracturing pressure increase of 90 bar.*
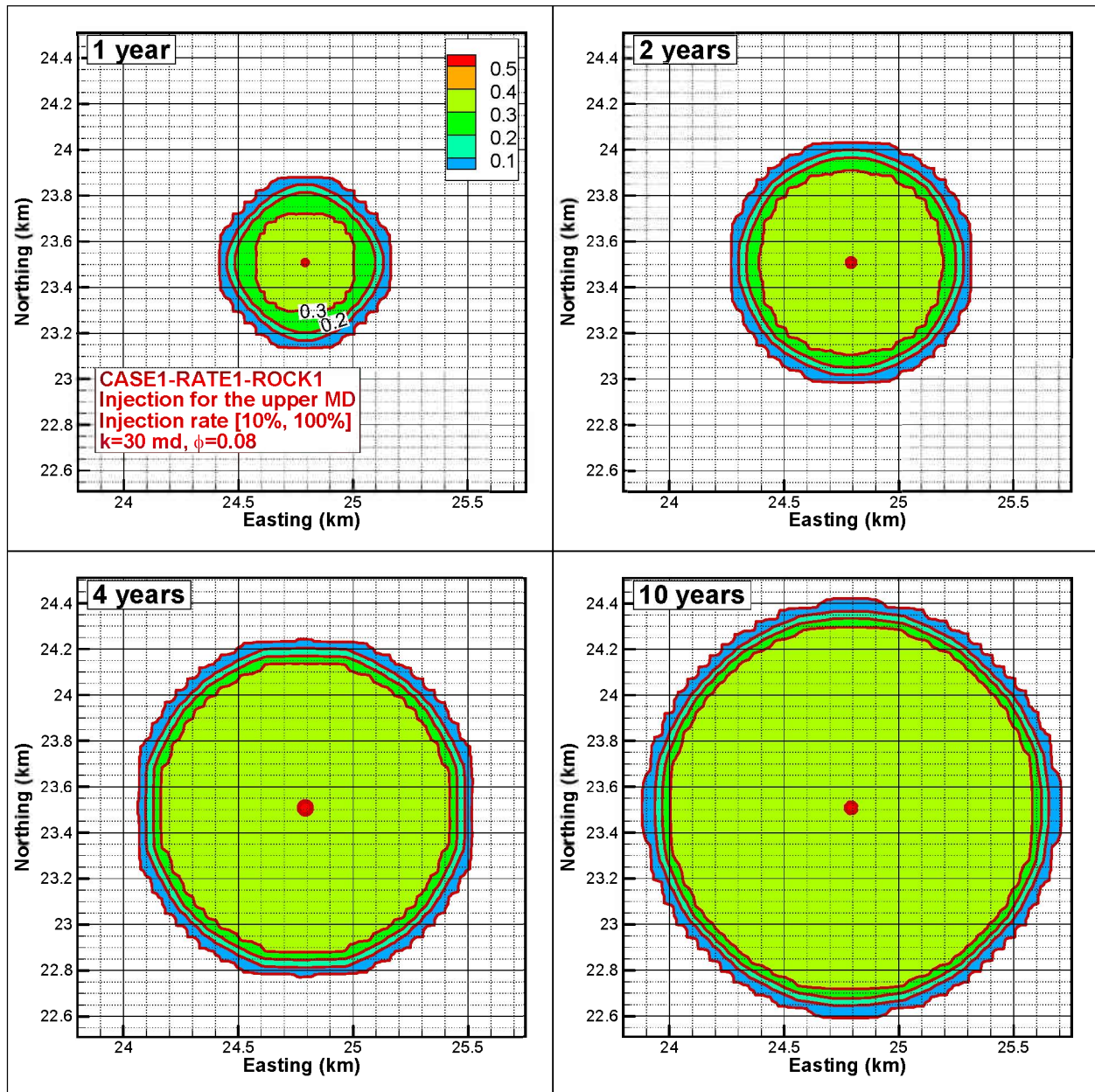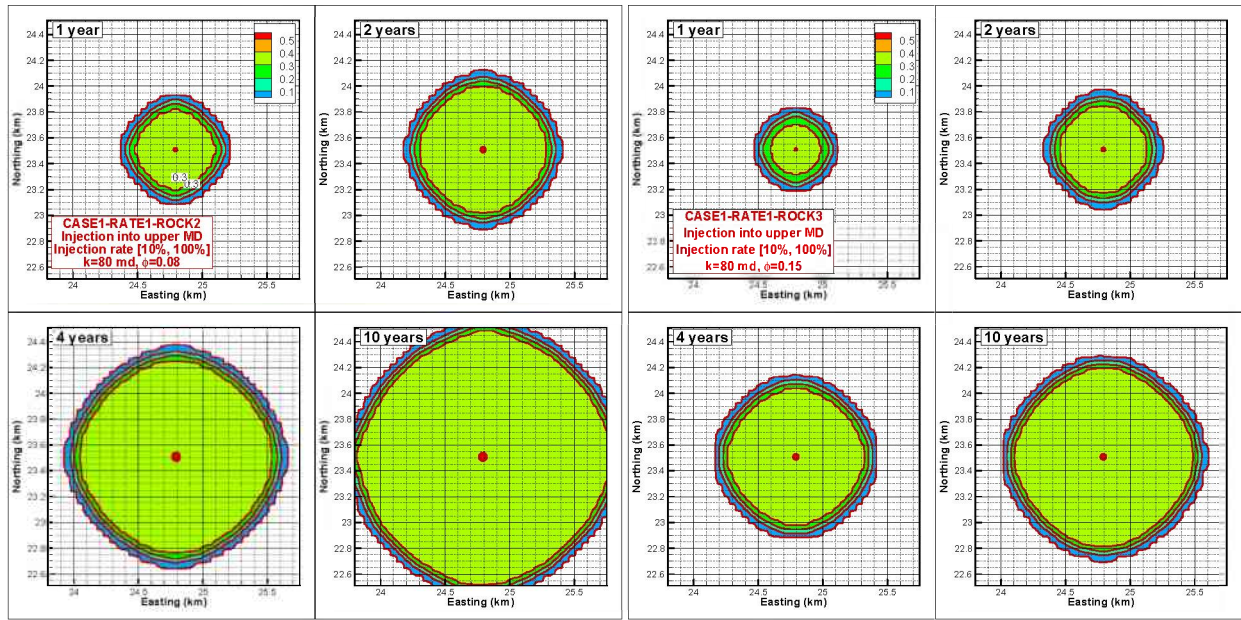
Figure 3.3-2. *Contours of simulated CO_2 saturation in the top model layer of the middle Duperow at 1, 2, and 4 years during the injection period, and 6 years during the post-injection period for cases ROCK2 and ROCK3.*
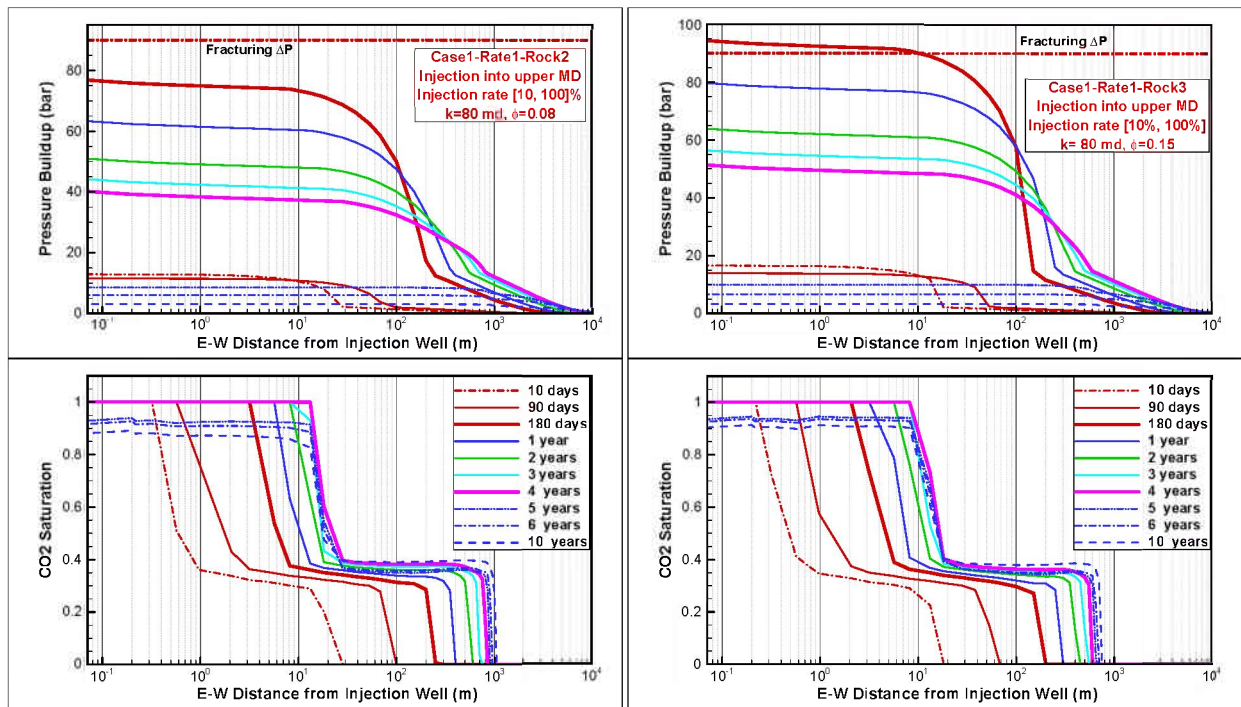
Figure 3.3-3. *The east-west profiles of pressure buildup and CO_2 saturation at the injection well as a function of time for cases ROCK2 and ROCK3.*

3.3.2. Effect of Injection Scenarios

As mentioned earlier, the injection schedule in the base case (RATE1) provides a step-up in rate over time, from a 10% design rate during the first 90 days, to a 100% design rate for the remaining injection time. To further investigate the step-rate injection scheme, we gradually increased the step rate in RATE2 as shown in Table 3.3-2.

Table 3.3-2. Step injection rate in injection scheme 2 (RATE2)

10% in [0,10d]	50% in [180d,1y]
20% in [10d,30d]	100% in [1y,3y]
30% in [30d,90d]	120% in [3y, 4y]
40% in [90d,180d]	

Simulations with RATE2 for cases ROCK1 and ROCK2 were conducted. The improved injectivity is shown in Figure 3.3-4, in comparison to the results with RATE1. Using the injection scheme RATE2, there is no injectivity issue during the first 90 days (when the injection rate is equal to or less than 30% of the design injection rate) in the base case of rock properties. With the increase in injection rate, the injectivity becomes an issue. However, ΔP is significantly less than those in RATE1. For example, the maximum ΔP is 160 bar at 4 years in RATE2, significantly lower than the maximum ΔP of 220 bar at 180 days in RATE1. For the second case of rock properties (ROCK2), the maximum ΔP with RATE2 at 4 years is 47 bar, higher than 40 bar at 4 years but lower than the maximum ΔP of 77 bar at 180 days in the case of injection scheme RATE1. All these results indicate that CO_2 injectivity can be enhanced using an injection schedule with gradual step increases in CO_2 injection rate.

Again, it is observed that the pressure buildup is mainly caused by two-phase flow effects in the two-phase region, in addition to pressure changes in the single-phase brine zone. In the RATE2 scheme, this two-phase zone develops gradually with smaller pressure buildup than in the RATE1 scheme1. Once the two-phase zone is sufficiently large, the additional pressure buildup with increase in injection rate is less than that with the same increase in injection rate at the very beginning of the CO_2 injection. This is because the very small CO_2 viscosity permits relatively large flow rates despite the small relative permeability of CO_2. The CO_2 saturation profiles for the two step-rate injection schemes in the case of ROCK1 are shown in Figure 3.3-5, along with the time-dependent injection rate and cumulative CO_2 mass injected.
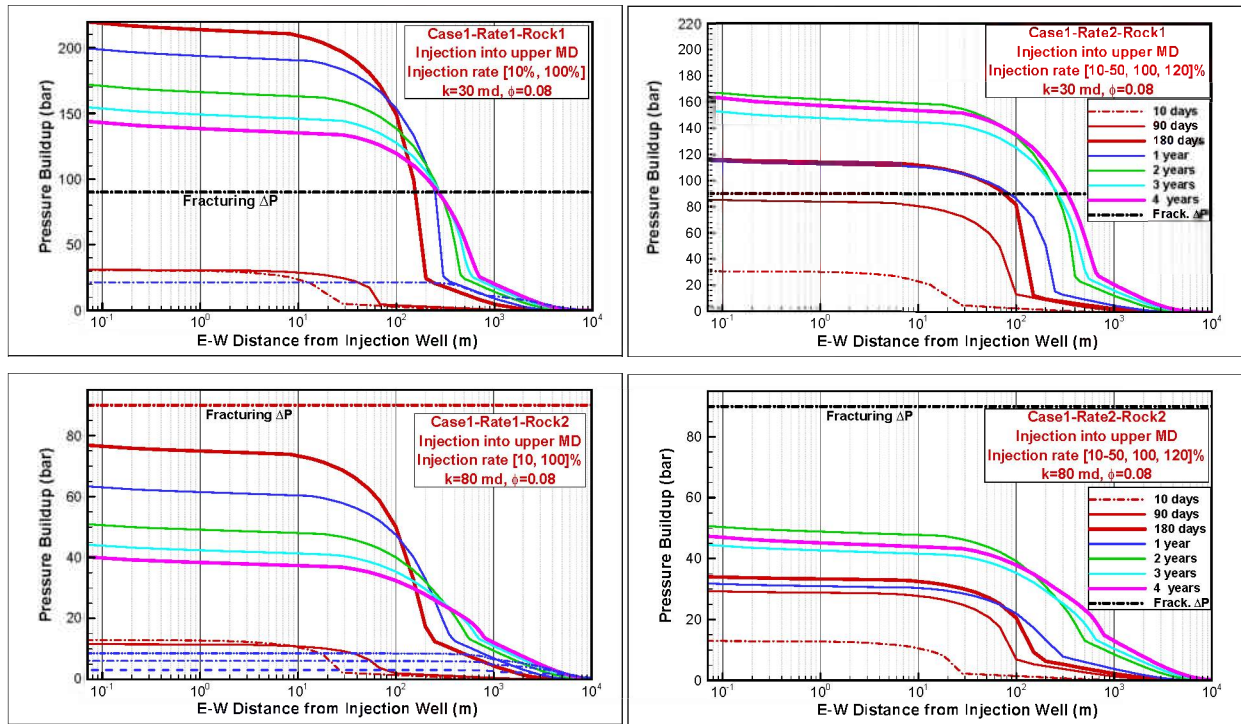
Figure 3.3-4. *The east-west profiles of pressure buildup at the injection well, as a function of time in both cases of injection scheme (RATE1 and RATE2) for the two cases of rock properties: ROCK1 and ROCK2*
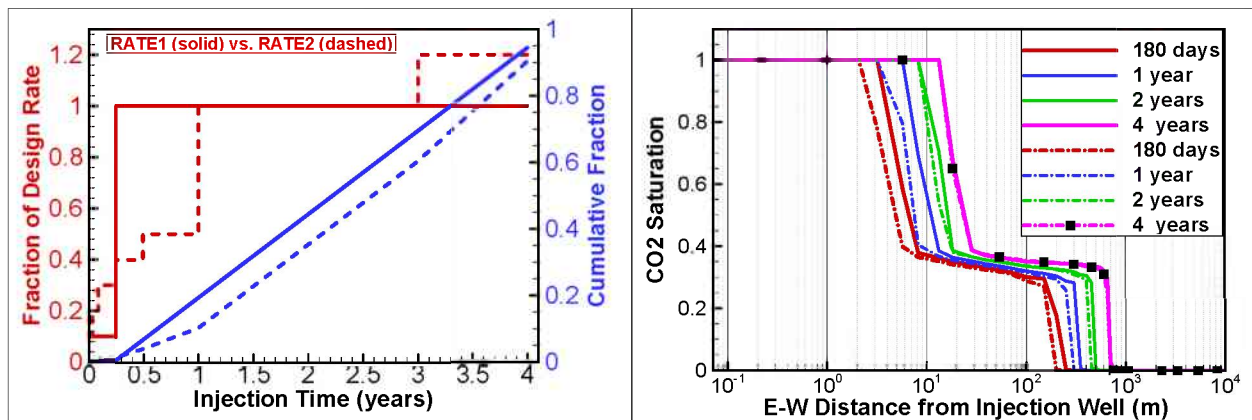
Figure 3.3-5. *Two injection schedules (RATE1 and RATE2) and cumulative fraction injected (left-hand side) with corresponding east-west profiles of CO_2 saturation through the injection well (right-hand side, as a function of time for RATE1 (solid) and RATE2 (dashed) for the ROCK1case of rock properties.*

3.4.   Conclusions

Two-phase CO_2-brine flow simulation was conducted to investigate the responses of CO_2 saturation and pressure buildup to CO_2 injection into the middle Duperow. A 3D flow model was developed on the basis of the 3D geological model provided by Schlumberger, by focusing on the 50 km × 40 km region approximately centered at the injection well. In the vertical direction, the 3D flow model consists of the Nisku formation and the upper Duperow unit as cap rock, the

middle Duperow as storage formation, and the intermediate and lower Duperow and Souris River formation as basement rock. The initial conditions used included the *in situ* pressure conditions (20 bar under hydrostatic pressure) in the middle Duperow and a moderate salt mass fraction of 0.13, and a temperature of 34.4 °C. At this stage of the Kevin Dome project, little is known about the rock properties (porosity and permeability) of the middle Duperow, as well as its two-phase flow properties. It was assumed that the porosity and permeability of the middle Duperow are 0.08 and 30 md, respectively, in the base case, with generic two-phase flow properties assumed. Sensitivity of permeability and porosity was analyzed.

The simulation results for the base case of rock properties point out some concerns about CO_2 injectivity, because the maximum pressure buildup is as high as 220 bar at the injection well. This maximum value is much higher than the assumed allowable (fracturing) pressure increase of 90 bar (170% fracturing pressure gradient plus the 20 bar underpressure). The significant pressure buildup can be attributed to the low permeability and relatively small CO_2 relative permeability in the two-phase CO_2-brine zone, which accounts for ~90% of the total pressure buildup at the injection well. When the permeability is increased to 80 md with porosity unchanged, the injectivity issue disappears, since the maximum pressure buildup is 77 bar during the 4 years of injection.

When there is an injectivity issue because of low permeability, the step-rate injection strategy can reduce pressure buildup by gradually increasing injection rate to compensate for dynamic relative permeability. This strategy was demonstrated by comparing an injection scheme of [10%, 100%] of design injection rate of 7.92 kg/s within [0, 90 days] and [90 days, 4 years] to a scheme of [10%, 20%, 30%, 40%, 50%, 100%, and 120%], with a constant step increase at 0 d, 10 d, 30 d, 90 d, 180 d, 1 year, and 3 years. The latter scheme can enhance CO_2 injectivity to a certain degree, but cannot completely avoid the injectivity issue for the base case of a permeability of 30 md and porosity of 0.08 in the middle Duperow.

4. MULTIPHASE FLOW MODELING FOR CO_2 PRODUCTION

4.1. Introduction

Critical to the success of the BSCSP Phase III project is the availability of a large amount (at least 1 Mt) of high-quality CO_2 delivered at a rate of approximately 250 Kt/yr for four years to the injection well. The BSCSP located its Phase III project at Kevin Dome, a large natural source of CO_2. Although there is large confidence in the presence of CO_2 in the Duperow formation at Kevin Dome, there is uncertainty about the rates at which CO_2 can be produced from vertical wells completed in the Duperow. This uncertainty is managed in the project by budgeting for multiple CO_2 production wells, if needed. In order to determine the flow rate(s) from any new production well(s) in the Duperow, or the number of wells needed, the well(s) will need to be tested, a process that will involve venting CO_2 to the atmosphere. The project aims to maximize the amount of information gathered during flow-rate testing while minimizing the amount of CO_2 that needs to be vented.

In order to begin to address the above basic design issues impacting the needs of CO_2 production infrastructure at Kevin Dome, we undertook 3D multiphase flow modeling of CO_2 production including coupled wellbore-reservoir flow effects. We built the model domain on the existing 3D flow model grid and used the same hydrologic properties for the base-case scenario (see Section 3), adding a wellbore to enable modeling of wellbore-reservoir coupling. The approach we use is numerical simulation with the TOUGH codes (Pruess et al., 1999, 2011). Specifically, we used the newly developed T2Well/ECO2H code (Pan and Oldenburg, 2013) to simulate fully coupled wellbore-reservoir flow processes under non-isothermal, two-phase (CO_2 and brine) conditions for three components (H_2O, CO_2, and NaCl). ECO2H is a high-temperature version of ECO2N (Pruess, 2005). The results summarized here are preliminary and subject to revision and extension, depending on project needs and priorities.

4.2. 3D Coupled Wellbore-Reservoir Model of CO_2 Production

4.2.1. Model Domain and Mesh

For the coupled wellbore-reservoir CO_2 production simulations, we extracted (from the 50 km × 40 km 3D model grid—Section 3) a subdomain grid with dimensions 9 km × 7 km around the production well (red square in Figure 4.2-1). The production well is located at (1459277', 660149'), which converts to (22787.6296 m, 15213.4152 m) in the modeling coordinates. In the vertical direction, the model domain spans the vertical section between the top of the Nisku and the bottom of Souris River. The same static geological model is used as described in Section 2.3.

In the vertical direction, the middle Duperow is divided into two regions, I and II. The wellbore is assumed to penetrate from the top to bottom of the middle Duperow but is only perforated in the middle Duperow (I). Because the reservoir temperature is just a few degrees above the CO_2 critical temperature, it is possible that two-phase conditions for CO_2 (co-existence of liquid and gaseous CO_2) could occur in the upper levels of the production wellbore as decompression cooling occurs. This could lead to three-phase conditions, i.e., brine, liquid-CO_2, and gaseous CO_2, which is beyond the capability of the wellbore flow model and the equation of state in T2Well/ECO2H. To avoid possible three-phase conditions, we simulate only flow *up* the wellbore to a depth of 932.7 m, which is at the top of the Nisku. Despite this lack of a complete

wellbore, we still capture the basic wellbore-reservoir coupling process in the Middle Duperow (I).
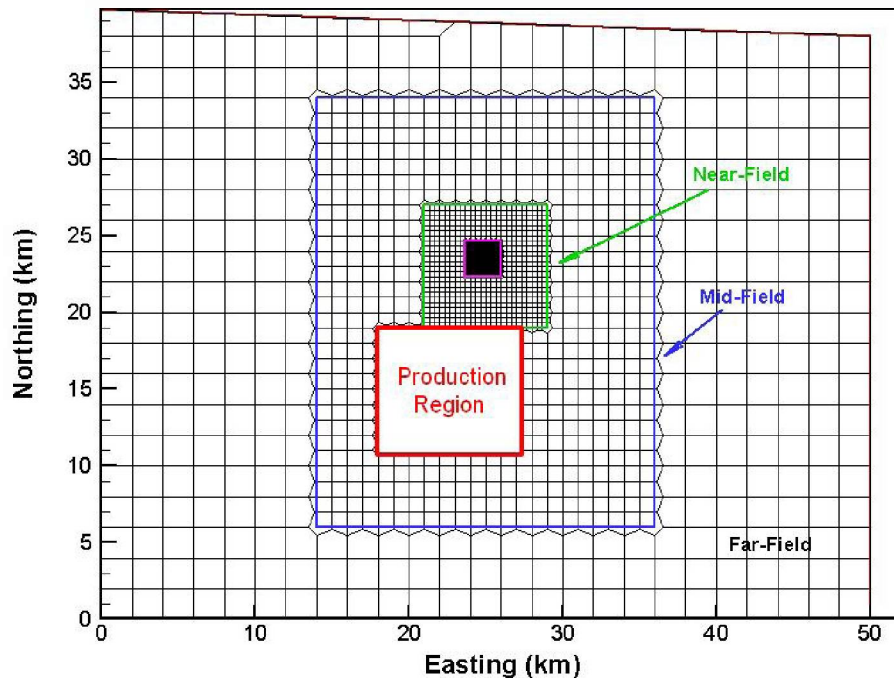
Figure 4.2-1. *The location of the production subdomain used in the wellbore-reservoir simulations.*

A 3D grid containing a single production well was generated using WinGridder (Pan, 2003) for the model. As shown in Figure 4.2-2 on the top surface displayed, the plan form of the grid honors the expected radial flow of fluids toward the well. The diameter of the wellbore (0.1397 m, or 5.5 in) is discretized exactly in the grid. The horizontal grid discretization increases from 0.1 m near the well to 500 m in the far field. Six hydrostratigraphic units around middle Duperow are included in the model, represented by 40 grid layers. The connections between wellbore cells and formation cells are set to be heat-conductive-only (i.e., no fluid flow), except in the Middle Duperow, where the well is perforated. The mesh has 28,320 grid cells.
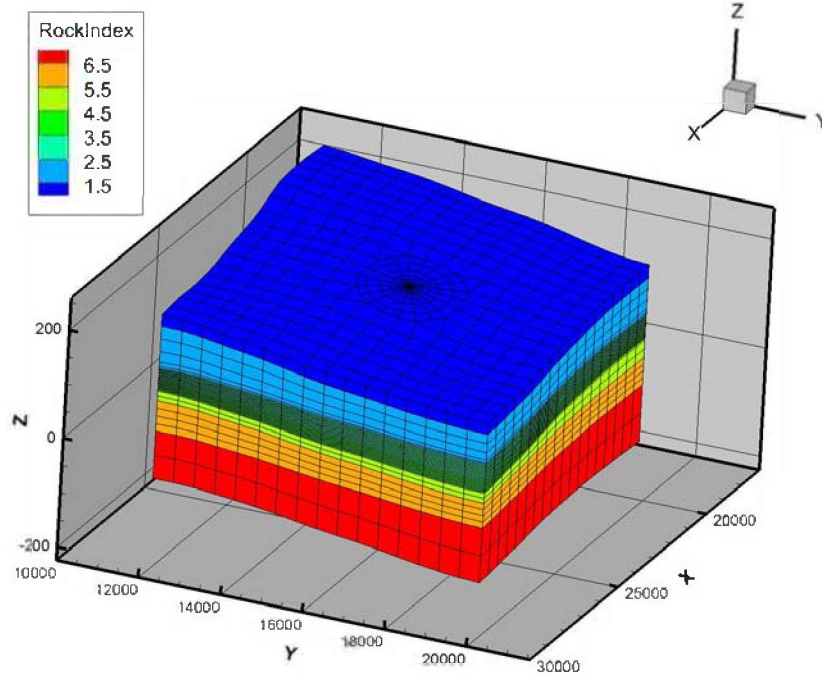
Figure 4.2-2. *3D grid of the production region model domain. Note the radial pattern in the top surface displayed. Horizontal grid discretization increases gradually from 0.1 m near the wellbore (well radius = 0.06985 m) to 500 m in the far field. The vertical discretization for the middle Duperow (so-called porosity layer) is about 2 m.*

4.2.2. Initial and Boundary Conditions

Initially, a normal hydrostatic pressure gradient and temperature linear with elevation are assumed (Table 4.2-1). All layers other than middle Duperow are filled with CO_2-saturated brine (NaCl mass fraction = 0.13). A horizontal gas-water contact between gas (CO_2-rich) phase and aqueous (brine) phase is defined within the middle Duperow. Because of uncertainty in the location of the gas-water contact, if one exists, we consider three cases of initial gas saturation, as shown in Table 4.2-2. Figure 4.2-3 shows the initial distribution of the gas phase (CO_2-rich phase) for the three cases. The hypothetical observation points (at which pressure will be reported in subsequent figures) are distributed at the top of the middle Duperow along a line to the east (positive x) of the production well (intersection of the two cross-sectional planes in Figure 4.2-3). All boundaries of the domain are assumed to be closed during CO_2 production, while a specific production mass flow rate is specified in the well (depth of 944.35 m).

Table 4.2-1. *Elevation-dependent initial pressure and temperature distribution*

Parameter	Value
Reference elevation (m)	95.423 (= 1005.84 m in depth at production well)
Temperature at reference elevation ($^\circ$C)	31.67
Pressure at reference elevation (MPa)	9.845713
Geothermal gradient ($^\circ$C/km)	24.46
Pore pressure gradient (MPa/km)	9.794718

Table 4.2-2. Initial gas phase distribution

Case	Depth of the gas-water contact (m)	Gas saturation above the gas-water contact
1	1100	0.9
2	1075	0.9
3	1050	0.9

(a)

(b)

(c)
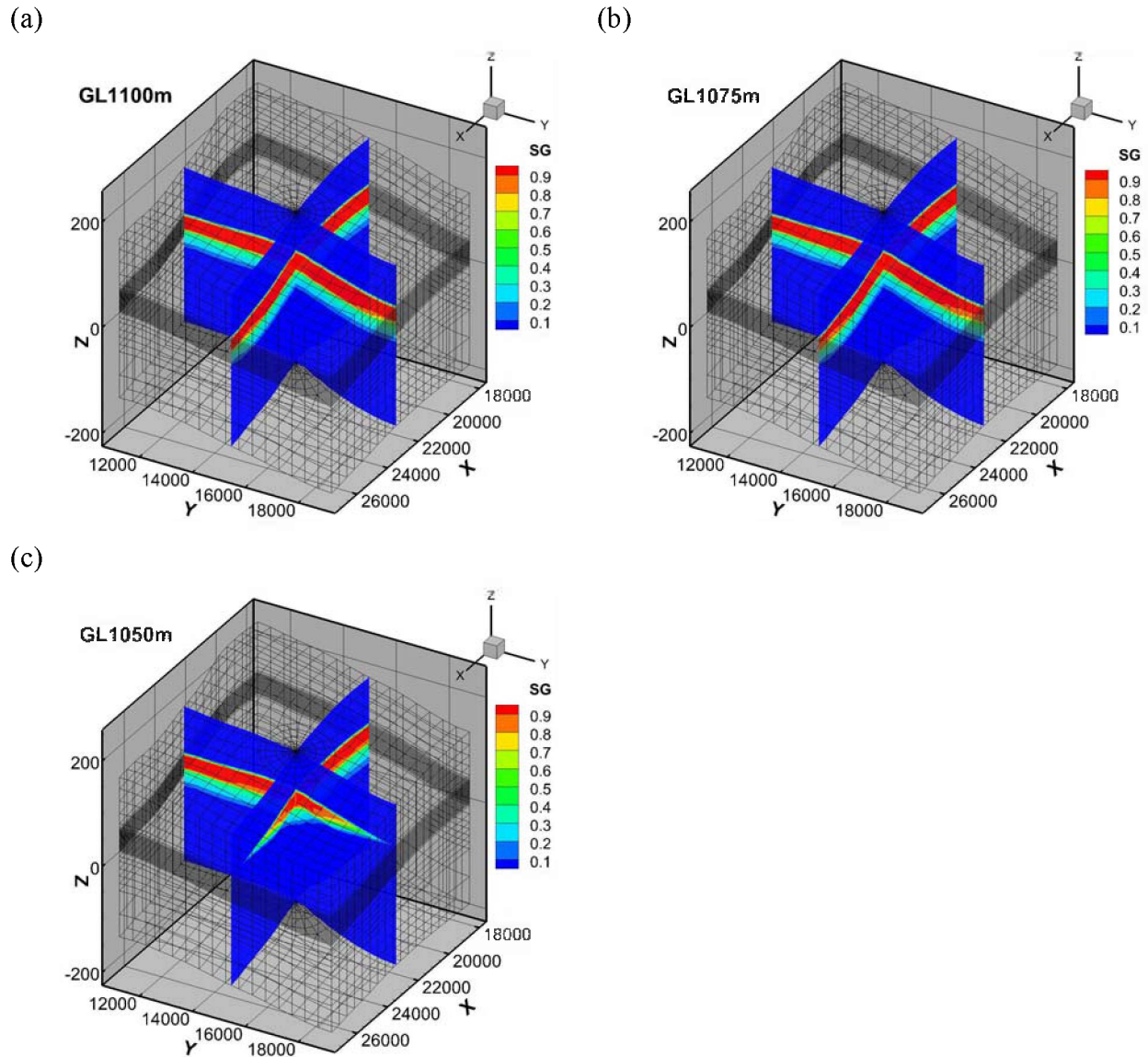
Figure 4.2-3. Initial distribution of CO_2 (along two cross sections that intersect at the production well) along with mesh. The color contour shows gas (CO_2-rich phase) saturation. The gas-water contact elevation is located at (a) 1100 m (Case 1), (b) 1075 m (Case 2), and (c) 1050 m (Case 3). The hypothetical observation points at which pressure will be reported are distributed at the top of the middle Duperow east (positive x) of the production well.

4.2.3.   Formation Properties

The formation properties are shown in Table 4.2-3, and are the same as in Section 3, as used for modeling CO_2 injection.

Table 4.2-3. Formation parameters

Formation	Nisku	Upper Duperow	Middle Duperow (I)	Middle Duperow (II)	Intermediate Duperow	Lower Duperow	Souris River
Permeability (m^2)	10^{-19}	10^{-17}	3×10^{-14}	2.5×10^{-16}	10^{-17}	10^{-17}	10^{-19}
Porosity	0.05	0.06	0.08	0.06	0.05	0.05	0.05
Heat conductivity (W/m °C)	2.51						
Rock grain density (kg/m^3)	2600						
Rock grain specific heat (J/kg °C)	920						
Pore compressibility (Pa^{-1})	1.628×10^{-9}						
Parameters for relative permeability (liquid relative permeability using van Genuchten-Mualem model (1980) and gas relative permeability using Corey model (1954))							
Residual gas saturation	0.25						
Residual liquid saturation	0.30	0.50	0.50	0.50	0.30	0.30	0.30
Saturated liquid saturation	1.0						
m$_{VG}$	0.457						
Parameters for capillary pressure (Capillary pressure using van Genuchten (1980) model)							
Characteristic capillary pressure (Pa)	10^7	2.5×10^5	1.25×10^4	2.5×10^5	2.5×10^5	10^7	10^7
Maximum capillary pressure (Pa)	10^8	10^8	10^6	10^6	10^8	10^8	10^8
Residual liquid saturation	0.25						
Saturated liquid saturation	0.999						
m$_{VG}$	0.457						

4.3.   Results and Discussion

4.3.1.   Influence Range of Production-Induced Pressure Perturbations

In this first simulation, we investigate the degree to which flow rate and flow time affect the penetration of pressure in the reservoir over time. The motivation for this set of numerical experiments is to ascertain whether flow test duration and associated CO_2 venting can be minimized, while learning the maximum amount about long-term deliverability, where long-term deliverability at a fixed rate depends on size and permeability of the reservoir. To this end, we have simulated a scenario of varied production rates starting at 2 kg/s, then increasing to 4 kg/s and 8 kg/s (the design rate equal to 1 Mt/4 yrs) sequentially, each for 10 days. The schedule then switches to 6 kg/s for 30 days followed by a total shut-in. As shown in Figure 4.3-1, pressures respond quickly to the flow rate change near the wellbore (observation point 0.00 m in Figure

4.3-1). However, far from the well, e.g., at the observation point 1078.75 m in Figure 4.3-1, the production-induced pressure perturbation is negligible during this 60-day period of production. With most simulated production rates, the pressure in the wellbore quickly reaches a quasi-steady state (leveling out of the pressure curve in Figure 4.3-1) except for the case of the 8 kg/s flow rate, in which the wellbore pressure is still undergoing a significant decrease after 10 days (from t = 20 to 30 d). The system is able to recover the pressure quickly after 60 days of production.
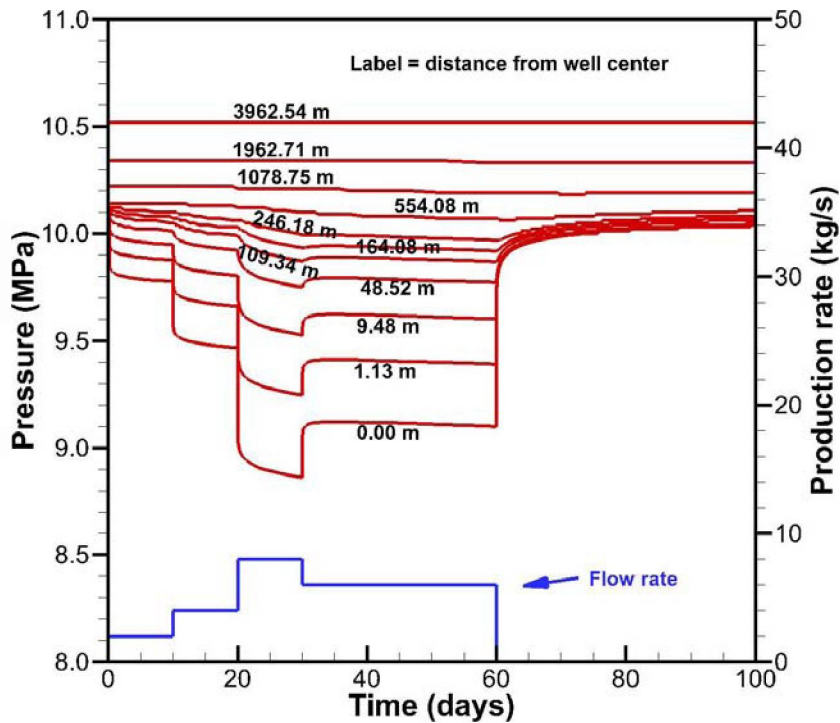
Figure 4.3-1. *Pressure (the red lines) at different distances (observation points) east of the production well in response to the varied CO_2 production rate (blue line). The pressures are reported in the topmost grid cell of the middle Duperow layer. Distance of 0.0 m indicates to the corresponding wellbore cell. The initial conditions are as in Case 1.*

The degree of pressure-signal penetration into the formation depends on duration of the production period. As shown in Figure 4.3-2, in the case of a three-day test with only one day each of different production rates, the pressure perturbation reaches a much smaller distance (< 250 m). Determining long-term deliverability will require perturbing a large radius of the reservoir.
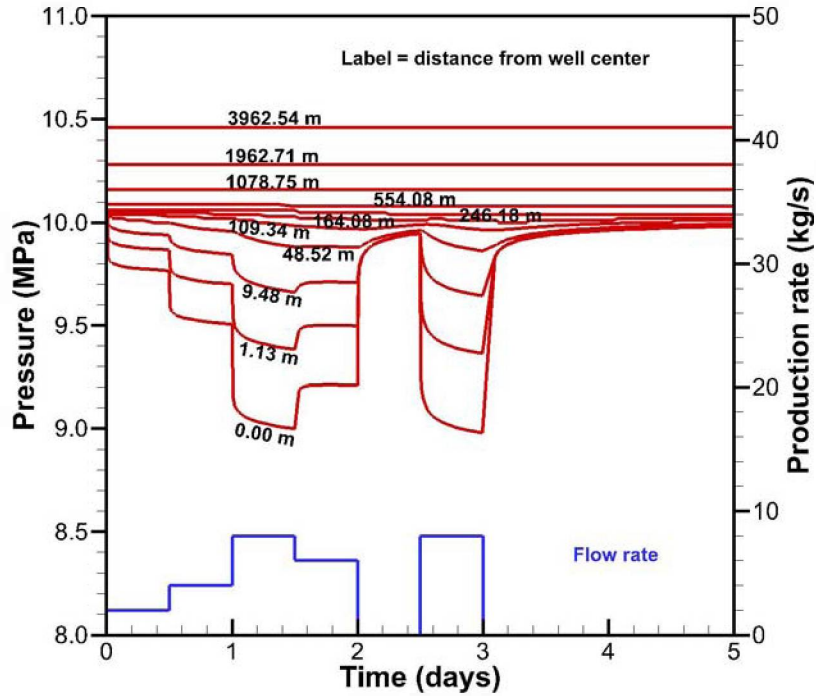
Figure 4.3-2. *Pressure (the red lines) at different distances from the production well (to east) as responding to the CO_2 production at varied flow rates (blue line). The pressures are reported in the topmost grid cell of the middle Duperow layer. Distance of 0.0 m indicates to the corresponding wellbore cell. The initial conditions are as in Case 2.*

4.3.2. Effects of Formation Permeability on Production Pressure

We know the downhole (944 m below surface) pressure during production tests is sensitive to the permeability of the middle Duperow. To see this effect, we simulated production tests for a base-case permeability (Table 4.2-3), and for one-half and two times this permeability of the middle Duperow (I). As shown in Figure 4.3-3, the lower the permeability, the deeper the drop in wellbore pressure during production, and the slower the recovery after shut-in.
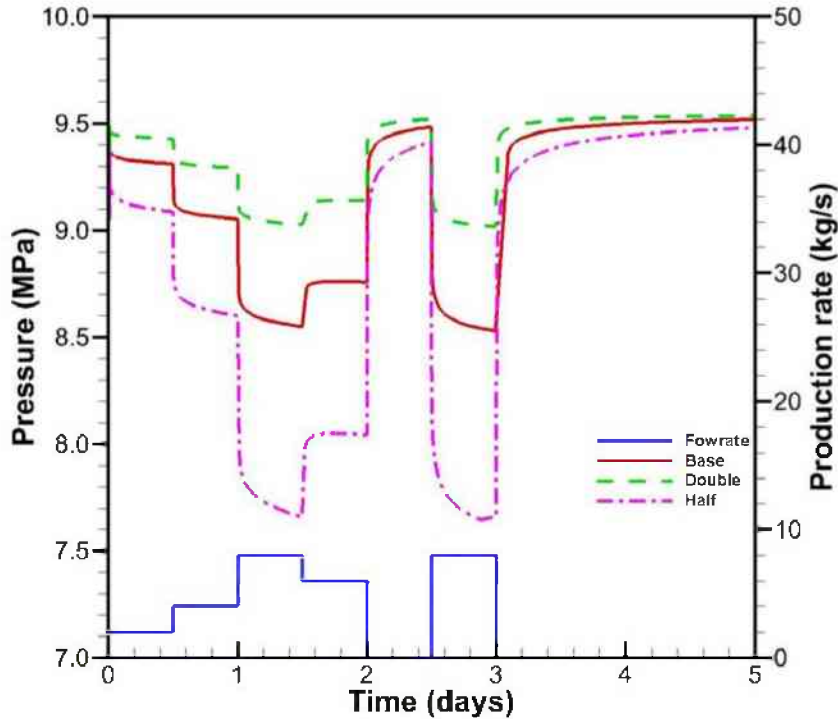
Figure 4.3-3. *Effect of the reservoir (middle Duperow I) permeability on the downhole (944 m below surface) pressure as response to the production rate (blue line). Permeability of base case is 3×10^{-14} m^2. "Double" and "half" indicate the cases that the permeability is doubled or halved from the base case, respectively. Initial conditions are as in Case 2.*

4.3.3.   Potential for Producing 1 Mt over Four-Years

Here, we consider the basic questions of (1) how much CO_2 can be produced from the reservoir over four years, and (2) how many production wells would be needed to maintain the desired total production rate. To answer these two questions definitively, one would need to know the reservoir configurations, formation properties, and the total CO_2 stored in the structure, i.e., one would need a detailed large-scale reservoir characterization, including results of a production test.

In the absence of detailed data on reservoir productivity, we have simulated a few cases assuming that the current static model is correct. We tried to test the possibility of producing 8 kg/s from a single well for four years (a steady production of 0.25 Mt/yr for 4 yrs), and to observe how the different initial conditions (Figure 4.2-3) would affect the production pressure. Figure 4.3-4 shows the downhole pressure during four years of production at 8 kg/s. Overall, the pressure drops as production continues, but the rate of pressure drop becomes smaller after early time. For all cases, production of 1 Mt/4 yrs from a single well appears possible, provided that the current estimated reservoir parameters and gas-water contact location are correct.

The depth of the gas-water contact has significant impact on the performance of the reservoir, because it defines the CO_2 capacity of the reservoir. For the same decrease of gas-water contact elevation (i.e., 25 m decrease), Case 3 shows a larger drop in pressure than Case 2, mainly because the gas-water contact is much closer to the production well in Case 3 than in Case 2. In

short, the volume of the reservoir containing CO_2 is smaller when the gas-water contact is shallower, and this manifests itself as a more rapid pressure drop.

To see the effects that brine flow has on CO_2 production, we have simulated a case with smaller residual brine saturation (i.e., brine is more mobile), modified from Case 3. As indicated by the "GL1050m_lowResi" label in Figure 4.3-4, the more-mobile brine flows toward the well and causes a larger pressure decline. Note that in all other cases, the brine is immobile for the given conditions (i.e., $S_L = 0.1$ and $S_{rL} = 0.5$).
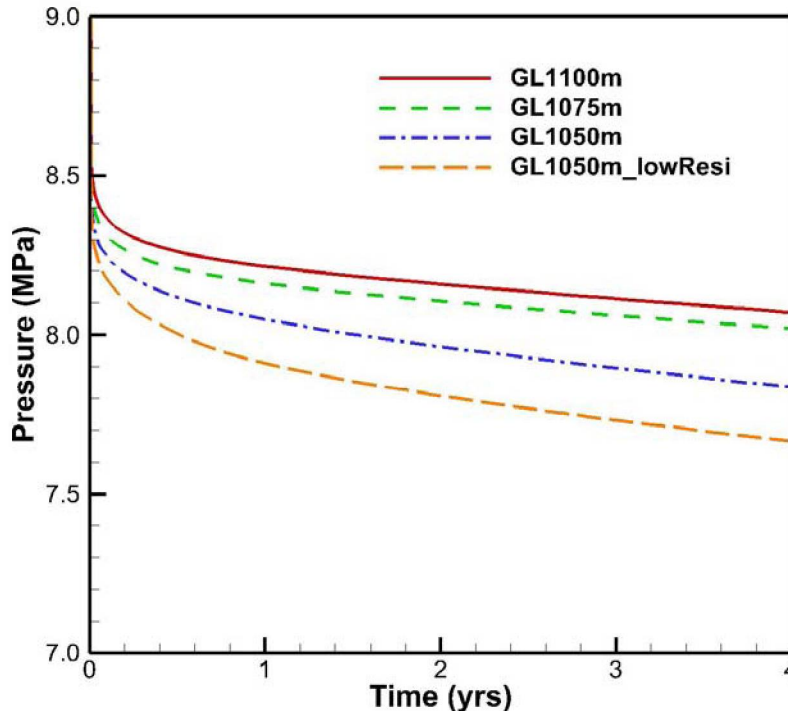
Figure 4.3-4. *Downhole (depth of 944m) pressures during four years of production at a rate of 8 kg/s for different cases. "lowResi" indicates that the residual water saturation of middle Duperow is 0.1 instead of 0.5 for other cases.*

4.4. Conclusions

Preliminary three-dimensional multiphase coupled wellbore-reservoir simulations have been carried out to investigate questions surrounding CO_2 production from the middle Duperow at Kevin Dome. The simulation domain is a subdomain of the larger Kevin Dome grid, discretized to include a 5.5-inch production well screened in the middle Duperow. Production flow tests show that single-well flow at rates near the 8 kg/s (1 Mt/4 yrs) design rate for 60 days produce a pressure signal that penetrates ~500 m into the dome. Production tests over a few days cause pressure to penetrate between 100 and 200 m into the middle Duperow. Higher reservoir permeability enhances deliverability, as expected. The location of the gas-water contact strongly controls CO_2 production, with shallower gas-water contact causing larger pressure drawdown for a given flow rate, due to the reduced gas volume of the reservoir. Potentially much more serious, a high gas-water contact could cause brine up-coning into the well. Our preliminary simulations

also suggest that mobility of water is an important factor affecting the productivity, which implies that information on capillary pressure and relative permeability, along with *in situ* water saturation in the gas reservoir, may be important parameters for accurately simulating CO_2 production.

5. GEOCHEMICAL AND REACTIVE TRANSPORT MODELING

5.1. Rock Composition

The sediment mineralogy assumed for the modeling studies is based on literature data, as discussed previously in Section 2.2.2.1. The various rock-forming minerals and their mass- or volume-fraction input into simulations are shown in Table 2.2-1. Major minerals consist of calcite, dolomite, ankerite and anhydrite, with minor amounts of quartz, illite/mica, and K-feldspar, and traces of pyrite, strontianite, and fluorite.

5.2. Brine Chemistry

An *in situ* brine composition (Duperow 2, Table 5.2-1) was reconstructed (TDS ~50,000 ppm, pH ~6.7) to reflect chemical near-equilibrium with the main formation minerals at *in situ* temperatures, and keeping elemental ratios in line with available data from the USGS-produced water database (e.g., Figures 2.2-4 and 5). Another more saline brine (~180,000 ppm, pH ~6.0) was also reconstructed (Duperow 3), but has not yet been used in modeling analyses. Note that the difference in salinity between these two brines is not expected to affect conclusions from the present modeling effort (i.e., conclusions of low reactivity).

In situ brine compositions were estimated starting from composition D (Table 2.2-1, sample 25001329), from a review of Duperow-formation brine compositions presented in Section 2.2.2.1. Using this water as initial composition, program GeoT (Spycher et al., 2011, 2013) was used to constrain the dissolved concentrations of key elements as shown in Table 5.2-1. The constraints were applied at the estimated temperature at a depth of injection (about 1000 m) at the site location (34 °C), which corresponds to a geothermal gradient of ~22°C/Km (Shepard, 1991), with an average surface temperature of 11°C. To avoid potential non-unique solutions when using multiple minerals to constrain dissolved concentrations of elements, we manually adjusted the concentrations of some elements to achieve equilibrium with known formation minerals and, iteratively, plotted the water composition on element correlation plots with all the available data for the Duperow formation in Montana (Figure 2.2-5), to ensure that the brine composition remained in line with other data from the Duperow formation.

Brine Duperow 2 was taken as our "base-case" composition and was essentially not concentrated relative to the samples labeled D in Table 2.2-2. However, the concentrations of some elements were adjusted to bring this brine at or close to equilibrium with the minerals shown on Table 5.2-1. Best results were obtained by adjusting the Ca and Mg concentrations to yield equilibrium with ordered dolomite. Sedimentary dolomite would be expected to be disordered; however, our thermodynamic data for disordered dolomite yielded Mg concentrations that appeared too high. This possibly could reflect uncertainty regarding the thermodynamic properties of this mineral. The bicarbonate concentration of the brine was not readjusted for possible CO_2 loss upon sampling (e.g., Palandri and Reed, 2001), because satisfactory results were obtained with the reported value, and also because the simulations consist of adding CO_2 to the system in amounts that largely exceed natural background concentrations. Acetate was added as a typical component of basin brine, at an arbitrary concentration in the range of typical values (e.g., Palandri and Reed, 2001 and references therein). The major cation and anion concentrations reconstructed in this manner fall close to the composition of the original samples considered (D samples of Table 2.2-2), and in line with other available data (Figures 2.2-3, 4, and 5). The more

concentrated brine Duperow 3 was constructed by concentrating brine Duperow 2 by a factor of 3 and keeping essentially the same mineral equilibrium constraints as for brine Duperow 2. This brine is not used with the present simulations, but may be used in ongoing modeling efforts.

Table 5.2-1. Reconstructed brine composition (Duperow 2) for geochemical and reactive transport modeling analyses.

Species	(molal)	(ppm)	Constraints or adjustments at T = 34 °C
pH 34 C	6.65	6.65	
pH 25C	6.71	6.71	Total H+ computed for equilibrium with calcite
Cl-	7.19E-01	25477	Charge balance
SO4-2	5.80E-02	5571	Equilibrium with anhydrite
HCO3-	3.21E-03	196	
HS-	2.86E-09	0.000	Equilibrium with pyrite
SiO2(aq)	2.75E-04	8	Equilibrium with chalcedony
Al+3	4.90E-10	0.00001	Equilibrium with kaolinite (initially k-spar)
Ca+2	5.00E-02	2004	Adjusted to yield close equilibration with dolomite
Mg+2	1.95E-02	474	Adjusted to yield close equilibration with dolomite
Fe+2	6.56E-06	0.3662	Equilibrium with ankerite
K+	2.37E-3	92	Adjusted for close equilibration with muscovite
Na+	7.06E-01	16230	
Sr+2	4.79E-04	42.0	Equilibrium with strontianite
F-	1.90E-04	4	Equilibrium with fluorite
B	3.86E-04	4.2	Estimated using Cl/B ratio in seawater
Br-	1.03E-03	82	Estimated using Cl/Br ratio in seawater
Acetate	1.00E-02	590	Arbitrary concentration in line with many basin brines
TDS		50401	

Computed mineral saturation indices as a function of temperature for reconstructed brine Duperow 2 are shown on Figure 5.2-1 and display close equilibration with the main formation minerals at 34°C. The assumption of equilibrium with these minerals is warranted on the grounds that their reaction rates are known to be fast (Table 5.3-1). Chalcedony is used to control dissolved silica concentrations, a good assumption because this phase is typically observed to control silica solubility in basin brines at temperatures below about 70°C (Kharaka and Mariner, 1989), because the quartz reaction rate at low temperature is extremely slow.

Note that the mineral assemblage presented in Table 2.2-1 and brine composition in Table 5.2-1 provide initial chemical conditions that were verified to remain essentially stable, for a period of at least 100 years, when simulating the natural system under kinetic reaction constraints prior to injection. Such a condition of initial quasi-steady chemical state is an important prerequisite for reactive transport simulations to ensure that water-rock interactions predicted during the period of CO_2 injection are related only to the effects of added CO_2, and not to fictitious effects from ill-conceived initial chemical conditions.
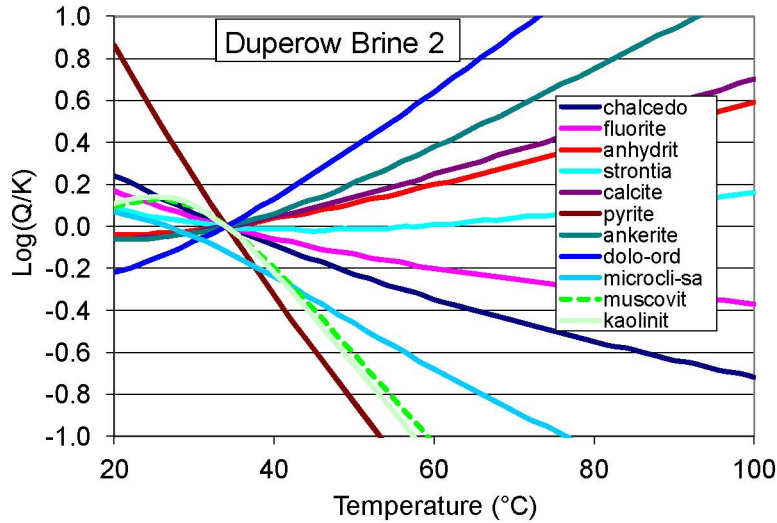
Figure 5.2-1. *Mineral saturation indices computed as a function of temperature for the reconstructed brine composition Duperow 2 shown in Table 5.2-1. Curves for the main formation minerals cluster near equilibrium at the assumed formation temperature of 34 °C.*

5.3. Thermodynamic and Kinetic Data

The thermodynamic database compiled by Reed and Palandri (2006) (soltherm.h06) was used in this study. This database relies on Gibbs free energy data primarily from Holland and Powell (1998) for minerals, and from SUPCRT92 (Johnson et al., 1992) for aqueous species. These data were updated using the data of Bénézeth et al. (2007) for dawsonite. (However, this mineral was found not to be thermodynamically stable in the modeled system.)

A general rate law derived from transition state theory (Lasaga et al., 1994) is used for mineral dissolution and precipitation:

$$R_m = \pm A_m k_m \left(\Omega_m^n - 1 \right)^p \tag{5.3-1}$$

where k_m is the rate constant (moles per unit mineral surface area and unit time), A_m is the specific reactive surface area per kg H_2O, Ω_m is the kinetic mineral saturation ratio (Q/K), and exponents n and p are either determined from experiments or taken equal to one. The value of the kinetic rate constant (k_m) can vary with the activity of other species, such as with pH (Lasaga et al., 1994; Palandri and Kharaka, 2004) as follows:

$$k = k_{25}^{nu} \exp\left[\frac{-E_a^{nu}}{R} \left(\frac{1}{T} - \frac{1}{298.15} \right) \right] + k_{25}^{H} \exp\left[\frac{-E_a^{H}}{R} \left(\frac{1}{T} - \frac{1}{298.15} \right) \right] a_{H^+}^{n_H}$$
$$+ k_{25}^{OH} \exp\left[\frac{-E_a^{OH}}{R} \left(\frac{1}{T} - \frac{1}{298.15} \right) \right] a_{H^+}^{n_{OH}} \tag{5.3-2}$$

where superscripts or subscripts *nu*, *H*, and *OH* indicate neutral, acid and base mechanisms, respectively; *a* is the activity of the species (in this case H+); n_H and n_{OH} are power terms (constant); and E_a is the activation energy for each mechanism.

These kinetic rate parameters were taken primarily from the compilation of Palandri and Kharaka (2004) and updated with data from Yang and Steefel (2008) for kaolinite, Hellevang et al. (2010) for dawsonite, and Golubev et al. (2009) and Duckworth and Martin (2004) for siderite (and applying the same data to ankerite), as shown in Table 5.3-1. Rates were assumed reversible, except for quartz, which was only allowed to dissolve. Chalcedony was included as a potential silica precipitation phase, using the rate law and data of Carroll et al. (1998) for amorphous silica.

Table 5.3-1. *Kinetic parameters for Equation 5.3-2, for k values in mol m^{-2} s^{-1} and Ea values in kJ mol^{-1}. See text for data sources.*

Mineral	$\log(k_H)$ (acid)	Ea_H (acid)	n_H	$\log k_{nu}$ (neut.)	Ea_{nu} (neut.)	$\log(k_{OH})$ (base)	Ea_{OH} (base)	n_{OH} (base)	$\log(k_{CO3})$ (carb.)	Ea_{CO3} (carb)	n_{CO3}
Quartz				-13.34	90.1						
K-feldspar	-10.06	51.7	0.5	-12.41	38	-21.2	94.1	-0.823			
Calcite	-0.3	14.4	1	-5.81	23.5				-3.48	35.4	1
Dolomite	-3.19	36.1	0.5	-7.53	52.2				-5.11	34.8	0.5
Pyrite	-7.52	56.9	-0.5 n_{Fe+3} 0.5	-4.55	56.9 n_{O2} 0.5						
Kaolinite*	-11.10	65.9	0.777		-12.97	-16.84	17.9	-0.472			
Anhydrite				-3.19	14.3						
Celestite	-5.66	23.8	0.109								
Muscovite	-11.85	22	0.37	-13.55	22	-14.55	22	-0.22			
Magnesite	-6.38	14.4	1	-9.34	23.5	-5.22	62.8	1			
Siderite	-3.75	48	0.75	-8.65	48						
Dawsonite	-4.48	49.43	0.982	-8.66	63.82						

* Re-fitted data; use with n = 0.333 in Equation 5.3-2

Input-specific surface areas used in the computation of A_m in Equation 5.3-1 were calculated assuming spherical grain sizes of about 0.2 mm for most of the minerals, yielding an input surface area value of 3×10^4 m^2/m^3 (on the order of ~10 cm^2/g, depending on density). For clay minerals (kaolinite and illite), these values were increased by a factor of 10. Note that because of the fast dissolution rate constants of the main rock minerals (calcite, dolomite, ankerite, anhydrite), the system quickly reaches equilibrium with respect to these minerals, and the model results are not expected to vary significantly with higher input surface areas.

5.4. Geochemical Modeling

The program CHILLER (Reed, 1982 and 1998) was used to conduct an analysis of brine-CO_2-rock chemical interactions under thermodynamic equilibrium constraints, for a closed system and without effects from flow and transport. This type of analysis was conducted to determine thermodynamic limits of reactions, type and stability of reaction products (secondary minerals), and initial rough estimates of porosity change and CO_2 mineral sequestration potential, under limits of thermodynamic equilibrium constraints. The simulations involved:

1. Saturating the brine-rock system with free-phase CO_2 at 34°C and 80 bar, up to a brine/CO_2 volume ratio in the range of typical CO_2 residual gas saturation (around 30%)
2. Reacting the low-pH brine/CO_2 system with the rock-mineral assemblage in incremental steps, up to a large brine-to-rock weight ratio of about 10:1.

At each reaction step, all thermodynamically possible reaction products (secondary minerals) were evaluated, and primary minerals that became (chemically) saturated no longer reacted with the brine/CO_2 system to mimic kinetic rates dropping to zero at equilibrium. Minerals that formed but did not belong on the basis of slow reaction kinetics at low temperature (e.g., high-temperature metamorphic minerals) were removed from the simulations.

This modeling analysis indicates that the brine+CO_2 mixture quickly attains equilibrium with all primary rock minerals, reaching a nearly constant pH near 5 and showing low reactivity and essentially no change in porosity (Figure 5.4-1). No new secondary minerals are predicted to form and K-spar alters to illite/mica phases. This can be explained by the self-limiting behavior of carbonate dissolution by CO_2, whereby addition of carbonic acid to the brine not only lowers pH, but also contributes dissolved carbonate that quickly keeps the brine from remaining undersaturated with respect to carbonate minerals, e.g.:

$$CO_{2(g)} + CaCO_{3(s)} + H_2O + 2H^+ \Leftrightarrow 2H_2CO_3 + Ca^{+2} \qquad (5.4-1)$$
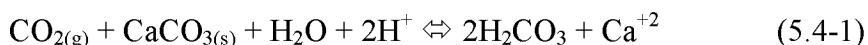
This reaction is hampered by the elevated initial calcium concentration in the brine (~2000 ppm), keeping the pH essentially constant near 5 at equilibrium with about 80 bar CO_2 at 34°C. Such pH buffering is further illustrated by the theoretical equilibrium boundaries of reaction 5.4-1 shown in Figure 5.4-2 (note that for simplicity this plot was drawn ignoring the dissociation of H_2CO_3, which would start to flatten the lines at pH above about 5.5; the non-ideal behavior of compressed CO_2 is taken into account, which collapses the boundaries at elevated P_{CO2}). This figure shows that as long as calcium concentrations remain elevated, the pH cannot increase. As a result, little reaction takes place, even at brine/rock ratios up to 10, and little CO_2 is mineralized. Such low reactivity appears consistent with a recent study showing essentially no difference in mineralogy between samples from the Duperow formation where natural CO_2 is known to be present and samples from the Midale formation at Weyburn (a mineralogical analogue) where natural CO_2 is absent (Ryerson et al., 2013). Note that carbonate minerals such as magnesite and dawsonite, which are often considered as potential sinks for CO_2, are computed to be thermodynamically unstable in this system over the entire modeled reaction interval. Additional modeling investigations (not shown) indicate that the extent of reactivity is tied to the amount of more alkaline silicate phases such as feldspar, micas, or clays (other than kaolinite) in the system. A greater amount of these minerals than modeled here would result in more reactivity, but would be untypical of the Duperow formation.
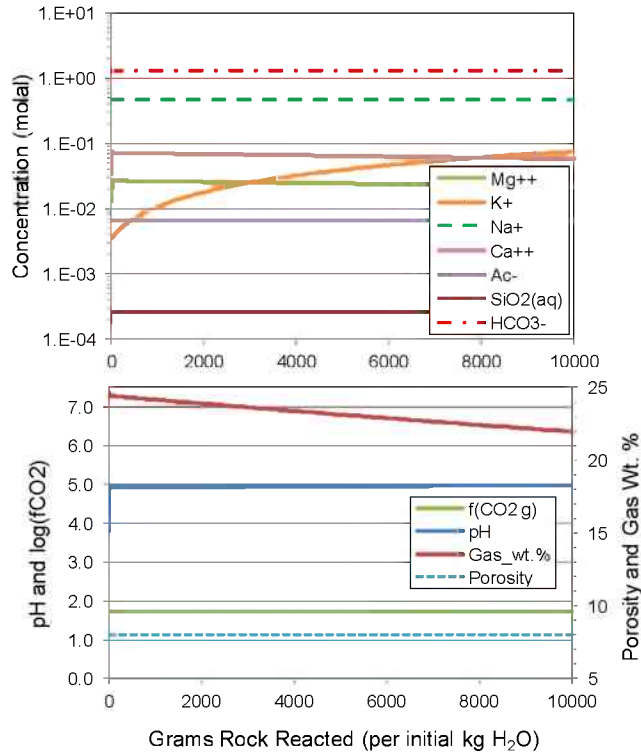
Figure 5.4-1. *CHILLER simulation of brine+CO_2 reaction with the Duperow formation mineralogy shown in Table 2.2-1 (closed system). Evolution of concentrations of main dissolved constituents. The assumed starting porosity is 8%. The initial pH of the brine+CO_2 mixture without rock is about 3.8. Potassium increases from K-feldspar dissolution until near equilibrium with illite/mica phases (modeled as muscovite). Other primary minerals remain at saturation over the entire reaction interval and no new phases form.*

Figure 5.4-2. *Calculated Ca activity and pH for reaction 5.4-1 (calcite dissolution) at thermodynamic equilibrium, as a function of CO_2 partial pressure. The dashed-line boundary indicates typical Ca concentration range in the brines of interest, buffering pH at low values near 5.*

5.5. Reactive Transport Modeling

In light of the findings from the geochemical modeling, program TOUGHREACT V2.0 (Xu et al., 2011) was used to simulate the injection of CO_2 into the Duperow formation under fully dynamic conditions and applying kinetic constraints to mineral reactions. For simplicity,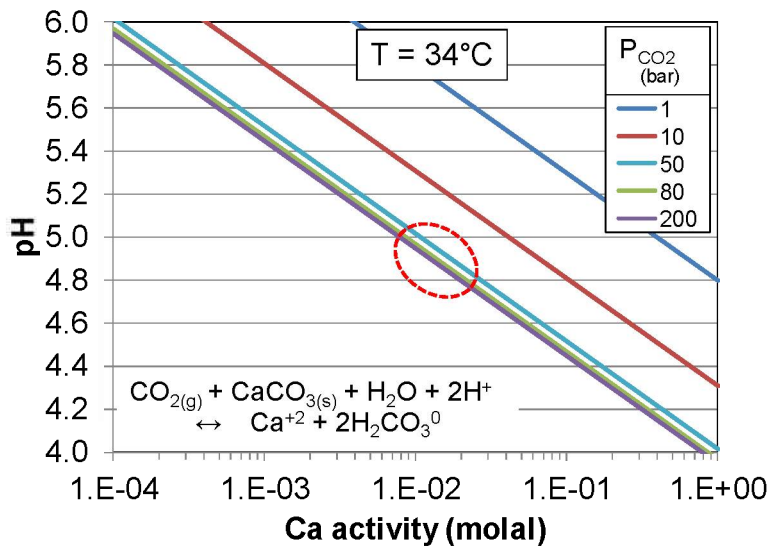 thermal effects of injection were not taken into account, because these effects are small and not expected to change the outcome of the reactive transport simulations. Also for simplicity, because the simulated geochemical system was found to operate mostly close to equilibrium with formation minerals, dissolution and precipitation rates were assumed to take the same value upon dissolution or precipitation, except for quartz, which was not allowed to precipitate (as discussed earlier).

A 2D vertical radial model was set up using hydrological parameters identical to those used in the base-case 3D flow model (Section 3.2). CO_2 injection was simulated into the Middle Duperow formation (~50 m thick, porosity 8%, permeability 3×10^{-14} m^2) interbedded between Intermediate/Lower Duperow units (~78 m thickness total, 5% porosity and 10^{-17} m^2 permeability) and Upper Duperow units (~64 m thick, 6% porosity, and 10^{-17} m^2 permeability).

The model boundaries were closed horizontally at the top of the Upper Duperow formation and at the bottom of the Lower Duperow formation, as well as vertically 10 km away from the injection well. It was verified from the 3D flow model that the vertical boundary is located far enough away from the modeled injection well to exclude significant boundary effects. The radial mesh was discretized into 4750 gridblocks, including 92 vertical grid spacings of 2 m each, and horizontal spacings starting at 0.11 m (approximately the borehole radius within the injection interval), then progressively increasing to a size no greater than 100 m within 1600 m from the injection point.

CO_2 was (numerically) injected at 0.25 Mt/y for four years, and the simulation continued for a period of time of 100 years from the start of injection. Time was discretized in increments varying from 1 second to no greater than about 11 days. Test simulations with smaller time steps (down to about 1 day) were also conducted, with similar results.

In contrast to the previous geochemical modeling analyses using CHILLER (Section 5.4), all minerals were considered to react under kinetic constraints, using the kinetic data shown in Table 5.3-1, and reactive surface areas estimated from assumed mineral grain sizes (Section 5.3). The precipitation and dissolution of minerals was coupled to porosity and permeability changes via a Carman-Kozeny model. However, as noted below, predicted changes in porosity were too small to affect permeability. The same thermodynamic data were used in the geochemical simulations. As noted earlier, because the system quickly reaches equilibrium with respect to the main primary minerals (which have fast reaction rates), long-term model results are not expected to be very sensitive to reaction rates (i.e., more reaction is not expected to occur with faster rate constants or larger surface areas, and slower kinetics would further lessen the predicted limited reactivity of the system).

Results of these preliminary reactive transport simulations are consistent with the previous geochemical modeling computations (Section 5.4). The injected CO_2 plume is predicted to extend to about 600 m from the injection well after 4 years (when injection stops), then to further

extend to a maximum distance of about 800 m, where it is predicted to remain for at least 100 years (Figure 5.5-1). The pH quickly drops to values near 4.9 and remains near this value for at least 100 years within a horizontal distance of about 500 m from the injection point (Figure 5.5-1). Calcite and dolomite are predicted to dissolve, and the resulting increase in dissolved calcium concentrations drives the precipitation of anhydrite. However, the amount of dissolution and precipitation of these minerals is very small ($< 10^{-4}$ volume fraction change, Figure 5.5-2) and as a result, the predicted porosity change is insignificant. K-feldspar is predicted to alter to illite/mica phases (modeled as muscovite) near the fringe of the CO_2 plume (Figure 5.5-3) where pH values are intermediate between the more acidic plume core and the background pH values near 6.7. However, the amount of reaction in this case is even smaller than for calcite, dolomite, and anhydrite. Small positive volume changes ($< 10^{-4}$) are also predicted near the wellbore from mineral precipitation due to evaporative concentration, because some water evaporates into the (dry) CO_2 near its injection point.

Figure 5.5-1. *TOUGHREACT simulation of CO_2 injection (1 Mt total) for a period of 4 years into the Middle Duperow formation: predicted compressed gas "liquid" saturation and pH at the end of the injection period and after a period of 100 years.*

It should be noted that predicted precipitation and dissolution amounts are typically sensitive to the time discretization in reactive transport simulations. In our case, simulations with time step sizes remaining near ~1 day resulted in an increased amount of precipitation (by up to 50%), however still much too small to impact porosity significantly.

Last, we should mention that siderite, magnesite, and dawsonite were included in the reactive transport simulations as potentially forming secondary phases. However, these phases were not

predicted to precipitate because they remained thermodynamically unstable, in agreement with the geochemical model presented earlier (Section 5.4). Consequently, essentially no CO_2 mineralization is predicted to take place, suggesting that solubility and residual saturation trapping are likely to be the main sequestration mechanisms at the site. As mentioned earlier, the lack of significant reactivity in this case is attributed to the self-limiting behavior of carbonate dissolution by CO_2 (reaction 5.3-1) which, at elevated calcium concentrations, keeps pH to values that are too low for secondary phases to form.
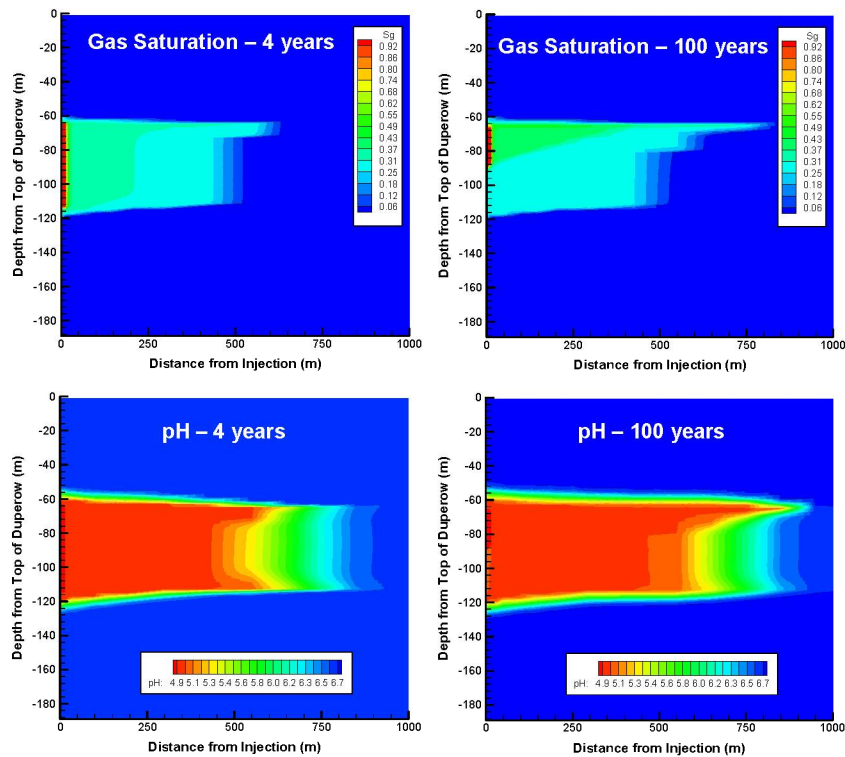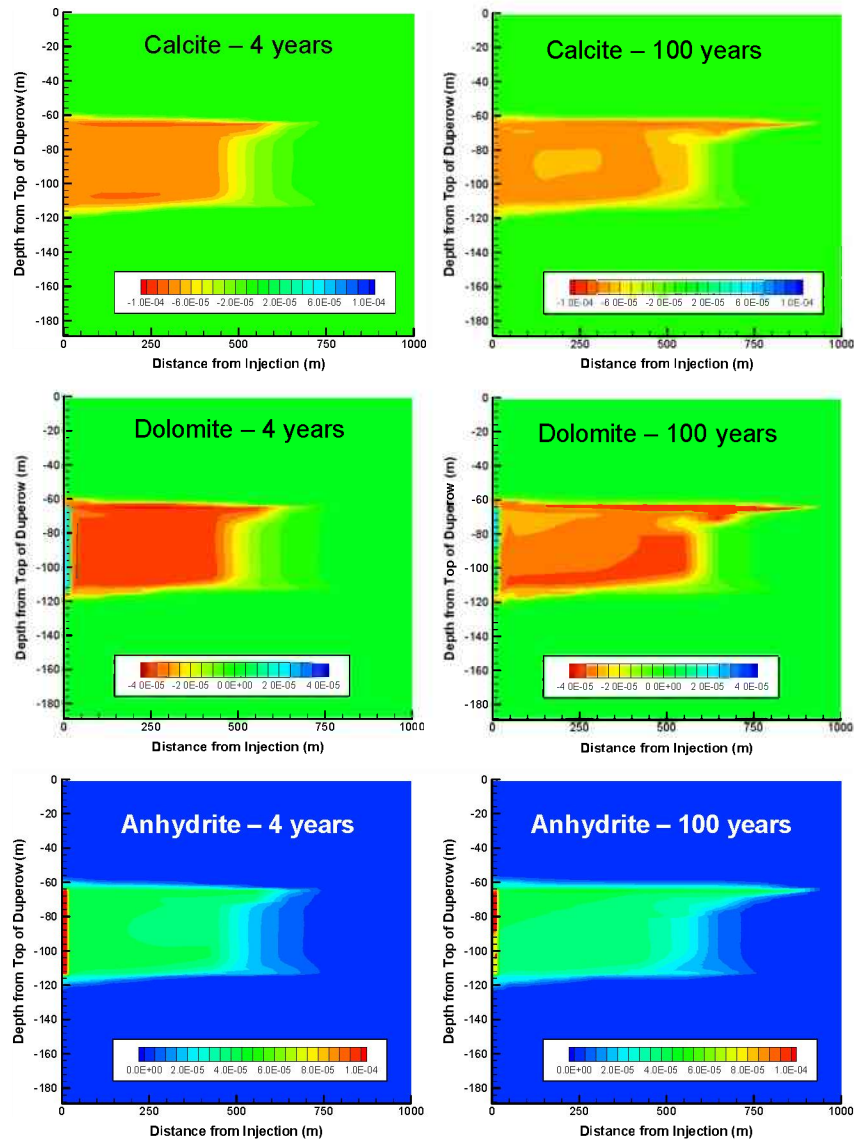

Figure 5.5-2. TOUGHREACT simulation of CO_2 injection (1 Mt total) for a period of 4 years into the Middle Duperow formation: predicted amounts of dissolution and precipitation of the most reactive minerals (in volume fraction change from initial conditions; negative for dissolution, positive for precipitation) at the end of the injection period and after a period of 100 years.

Figure 5.5-3. *TOUGHREACT simulation of CO_2 injection (1 Mt total) for a period of 4 years into the Middle Duperow formation: predicted alteration of K-feldspar to illite/mica (modeled as muscovite) in volume fraction change from initial conditions (negative for dissolution, positive for precipitation) at the end of the injection period and after a period of 100 years.*
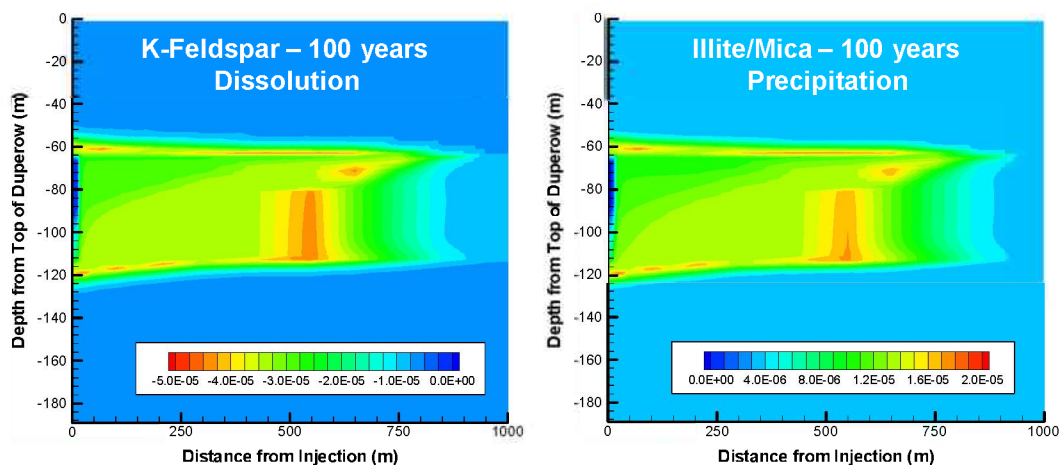
5.6.   Conclusions

Geochemical modeling was carried out by building up representative model rock and pore-fluid compositions from the literature and relevant databases. The initial chemical conditions based on these compositions were verified to remain stable for a period of at least 100 years. This period is an important prerequisite for reactive transport simulations to ensure that water-rock interactions predicted during the period of CO_2 injection are related only to the effects of added CO_2, and not to fictitious transient effects. Published thermodynamic databases and kinetic models, along with standard assumptions about mineral surface areas, were used to define kinetic controls on mineral dissolution and precipitation. Preliminary equilibrium geochemical modeling indicates that the brine+CO_2 mixture quickly attains equilibrium with all primary rock minerals, reaching a nearly constant pH near 5 and showing low reactivity with minerals present and essentially no change in porosity. Reactive flow and transport modeling of the CO_2 injection process, including full kinetics of the reactions, agrees well with the geochemical equilibrium modeling. This modeling shows that the pH quickly drops to values near 4.9 and remains near this value for at least 100 years within a horizontal distance of about 500 m from the injection point. Calcite and dolomite show minor dissolution, and the resulting increase in dissolved calcium concentrations drives the precipitation of anhydrite. However, the amount of dissolution and precipitation of these minerals is very small ($< 10^{-4}$ volume fraction change). The overall conclusion, based on available information and our geochemical modeling to date, is that reactivity is very low, with essentially no CO_2 mineralization predicted. The lack of significant reactivity is attributed to the self-limiting behavior of carbonate dissolution by CO_2, which, at elevated calcium concentrations, keeps pH to values that are too low for secondary phases to form.

6. MODELING IN SUPPORT OF AREA OF REVIEW

6.1. General Background

The Area of Review (AoR) is defined by US EPA (USEPA, 2010) as the region surrounding the geologic carbon sequestration project where USDWs may be endangered by injection activity. The AoR defines the area over which project operators or owners are required to identify potential leakage pathways (e.g., boreholes, faults, and fractures) that may need to be remediated. It also establishes the area where monitoring will need to be conducted. The area of review needs to be delineated using computational modeling that accounts for the physical and chemical properties of all phases of the injected CO_2 stream and displaced fluids—and is based on available site characterization, monitoring, and operational data. The AoR must be updated every five years unless a more frequent time period is required, based on monitoring data or other changes at the site.

The outer boundary of the AoR is defined by the largest of (i) the CO_2 plume boundary, (ii) the pressure front boundary, or (iii) the combination of the two over the duration of the project. Because geologic carbon sequestration in saline aquifers involves displacing relatively incompressible brine during CO_2 injection through wells, the aquifer pressure increases during injection. The pressure front caused by injection typically migrates much faster and farther than the injected CO_2 migrates. Because of this, the radius of the AoR around the injection well(s) is commonly controlled mostly by the pressure front, and the associated potential migration of brine from the injection zone upward into USDW. Specifically, for injection formations that are not overpressured with respect to the lowest USDW, EPA specifies that the radius of the AoR be defined by the minimum injection-zone pressure front ($P_{i,f}$) necessary to cause fluid flow from the injection zone upward into the formation matrix of the USDW, through a hypothetical conduit (i.e., artificial penetration) perforated in both intervals. This minimum injection-induced pressure (the so-called pressure front ($P_{i,f}$)) may be calculated from the following equation:

$$P_{i,f} = P_u + \rho_i \, g\left(z_u - z_i\right) \tag{6.1-1}$$

where P_u is the pressure in the USDW aquifer, ρ_i is the fluid density in the injection zone, g is the acceleration of gravity, and z_u and z_i are the reference elevations of the USDW and injection zone, respectively. Because the Class VI rule assumes an open conduit is present, this simple equation can be applied knowing only the pressure in the USDW (P_u), the density of brine in the injection zone, and the elevations of the USDW aquifer and the injection zone. Computational modeling provides the value of $P_{i,f}$ and associated radius to define AoR. Implicit in all of the above description is the assumption of normal hydrostatic gradients. A sketch of the conceptual framework upon which Equation 6.1-1 and AoR calculation rests is shown in Figure 6.1-1.
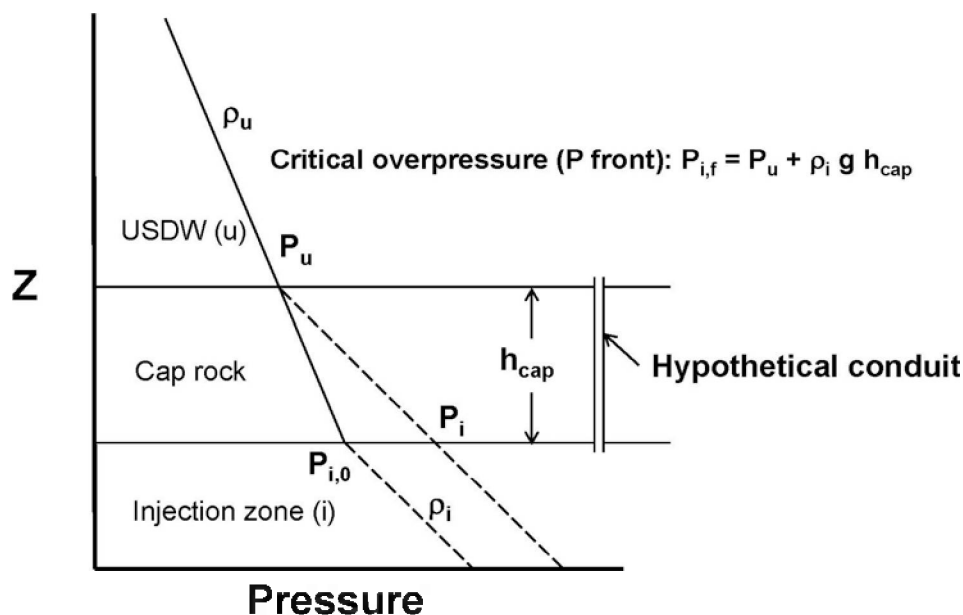
Figure 6.1-1. Sketch of the pressure profiles in USDW, cap rock, and injection zones typical of the conceptual model assumed by the EPA Class VI approach to AoR.

6.2. Preliminary Approach to Determine AoR at Kevin Dome

Our preliminary work in early 2013 on estimating AoR for the Kevin Dome project consisted of application of the standard approach of Equation 6.1-1, along with multiphase modeling to estimate $P_{i,f}$ as a function of radius, from which the radius of AoR could be determined using Equation 6.1-1. Even with a simple equation like Equation 6.1-1, with only four input values needed (P_u, ρ_i, z_u, and z_i), we were limited in making a precise estimate by lack of knowledge of the salinity in the injection zone, which controls ρ_i, to say nothing of uncertainties arising from the simulation results—which provide $P_{i,f}$ and which are highly dependent on the poorly constrained permeability of the Duperow injection zone. To make numerous rough calculations for ranges of values of uncertain parameters in Equation 6.1-1 (specifically, reservoir pressure, salinity, and to some degree elevations of the injection and USDW zone), we developed a spreadsheet model that used a standard estimate of brine density (McCutcheon et al., 1993) along with the EPA Class VI formalisms (e.g., Figure 6.1-1, Equation 6.1-1).

An image of the spreadsheet is shown in Figure 6.2-1. To use the spreadsheet model, the user provides input values of pressure, temperature, and salinity in the injection and USDW zones, along with cap-rock thickness (h_{cap}). The spreadsheet then calculates the water density and injection-zone pressure front ($P_{i,f}$), at which brine from the injection zone would be lifted up into the USDW zone.

As we began to work with colleagues at Montana State University (Fairweather and Bowen) in early spring 2013 to refine the spreadsheet model inputs (such as salinity, temperature, and pre-injection pressure in the injection zone and lower-most USDW), we determined from Drill Stem

Test (DST) data that both the Duperow injection zone and Madison USDW were underpressured. This can be seen in Figure 6.2-1, where by the calculated $P_{i,f}$ value of 8.6 MPa showing up in a red-colored cell, indicating that $P_{i,f}$ is smaller than $P_{i,0}$ (9.8 MPa), the initial injection zone pressure. A sketch of this situation is shown in Figure 6.2-2. We refer to this condition, in which the pressure front is smaller than the initial pressure, as pre-injection relative overpressure. In this condition, brine from the injection target zone would flow upward through a hypothetical conduit into USDW without any injection whatsoever. Clearly, the basis for the standard EPA Class VI AoR calculation is not consistent with this condition. This led to work on a revised approach, as discussed in the next section.
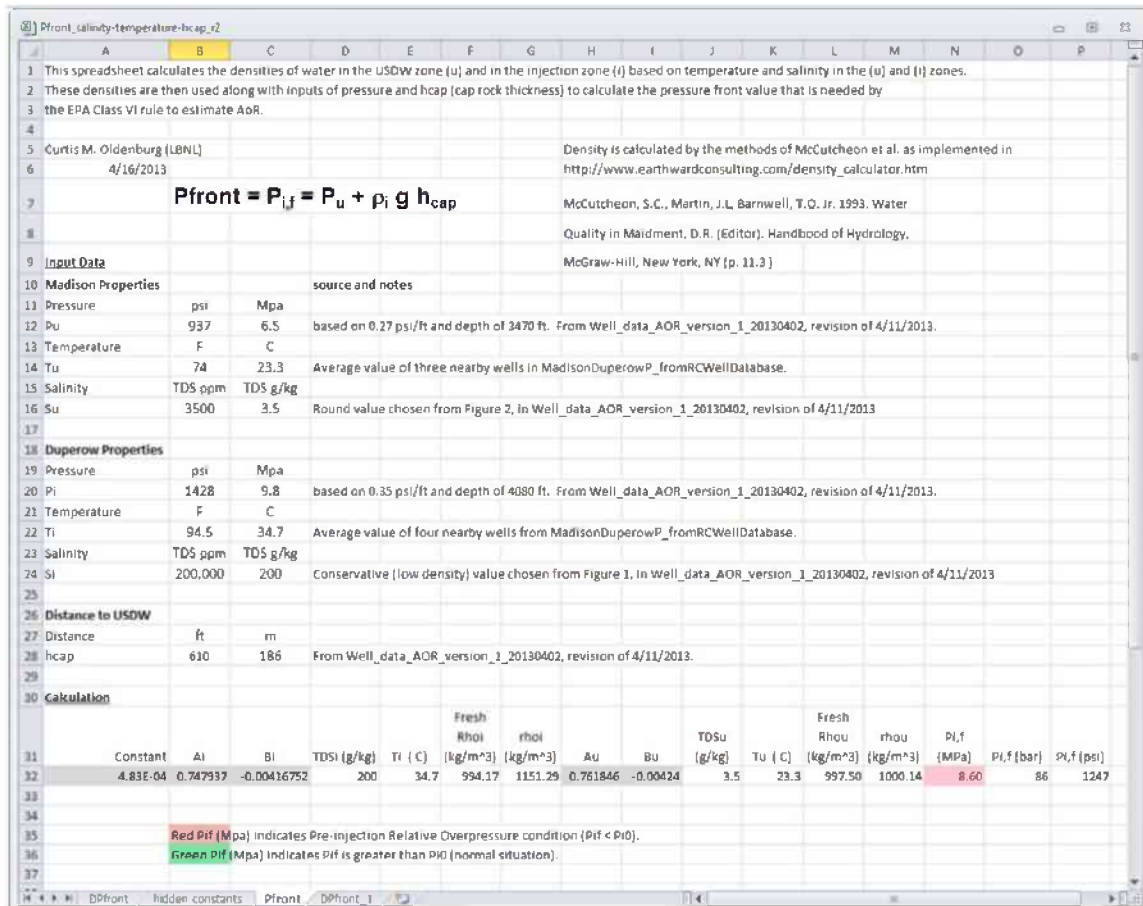

Figure 6.2-1. *Image of spreadsheet model developed to calculate AoR in conjunction with pressure perturbation obtained from flow simulation. This approach is only applicable when the injection and USDW zones are normally pressured (hydrostatic), as suggested by the red-green cell-color logic built in to the $P_{i,f}$ calculation.*

Critical P front:
$P_{i,f} = P_u + \rho_i \, g \, h_{cap}$

$T_u = 74\ ^\circ F = 23.3\ ^\circ C$
$P_u = 0.27\ psi/ft * 3470\ ft = 937\ psi = 65\ bar = 6.5\ MPa$
$TDS = 3500\ ppm \quad => \rho_u = 1000.1\ kg\ m^{-3}$

$T_i = 94.5\ ^\circ F = 34.7\ ^\circ C$
$P_{i,0} = 0.35\ psi/ft * 4080\ ft = 1428\ psi = 98\ bar = 9.8\ MPa$
$TDS = 200,000\ ppm \ => \rho_i = 1151.3\ kg\ m^{-3}$

$h_{cap} = 610\ ft = 186\ m$

$P_{i,f} = 6.5\ MPa + 1151.3*9.81*186 = 8.6\ MPa = 86\ bar$

Note that P_{i0} (the initial pressure) is equal to 98 bar, so we would actually have to reduce the pressure in the Duperow by 98-86 = 12 bar to avoid driving brine upward to the Madison.

Potential for upward brine flow to USDW is present prior to any CO_2 injection => *Pre-injection Relative Overpressure* condition
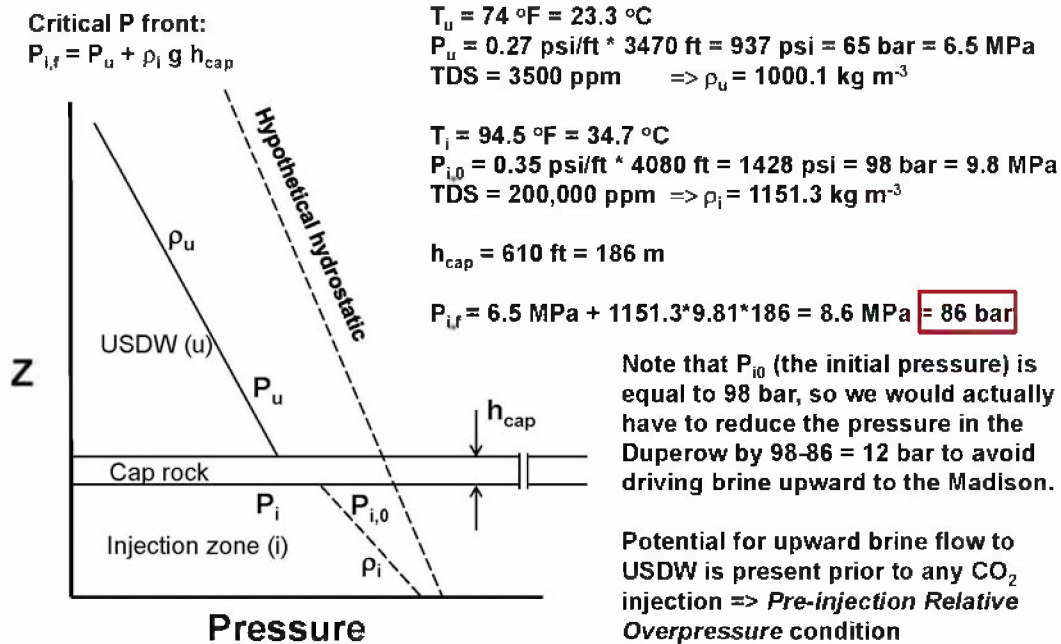
Figure 6.2-2. Sketch of pressure profiles for the Kevin Dome site along with assumed properties of the USDW and injection zones, and solution to Equation 6.1-1. See text for explanation.

6.3. Revised Approach to Determine AoR at Kevin Dome

As discussed above, the DST data suggest that the Duperow target CO_2 injection formation is in a pre-injection relative-overpressure condition, as sketched in Figure 6.2-2, meaning that without any injection whatsoever, brine would naturally flow upward through a hypothetical open well to the Madison formation, which is considered by EPA to be USDW (Underground Source of Drinking Water). This situation results in an infinite AoR, as calculated using the standard method of determination provided in the EPA Class VI guidance. Clearly, a revised approach was needed to calculate AoR.

In May 2013, the EPA released a revision to the Class VI guidance (USEPA, 2013) that includes specific approaches to addressing pre-injection relative overpressure. On p. 42 of the revised Class VI guidance, EPA stated that AoR can be defined by modeling the incrementally larger leakage rate that would arise through a hypothetical open borehole from the injection project, relative to the baseline (natural) leakage rate that would occur in the pre-injection relative overpressure situation, through that same hypothetical borehole with no injection project. At some distance from the injection well, specifically the AoR radius, the flow rate for the injection scenario would be larger than the baseline flow rate by an acceptable amount. The approach is shown schematically in Figure 6.3-1. The acceptably higher flow rate that would occur at a distance from the injection well equal to the AoR radius has yet to be determined in consultation with regulators. To prepare for these discussions, we modeled these flow rates as below.

2. A multiphase numerical model may be designed to model leakage through a single well bore, or through multiple well bores in the formation (see e.g., Birkholzer et al., 2011). Additional pressure increases up to a certain point within an already over-pressurized injection zone may not cause an appreciable increase in fluid leakage rates through a hypothetical borehole. A sensitivity analysis may be conducted to bound the modeled leakage rates.
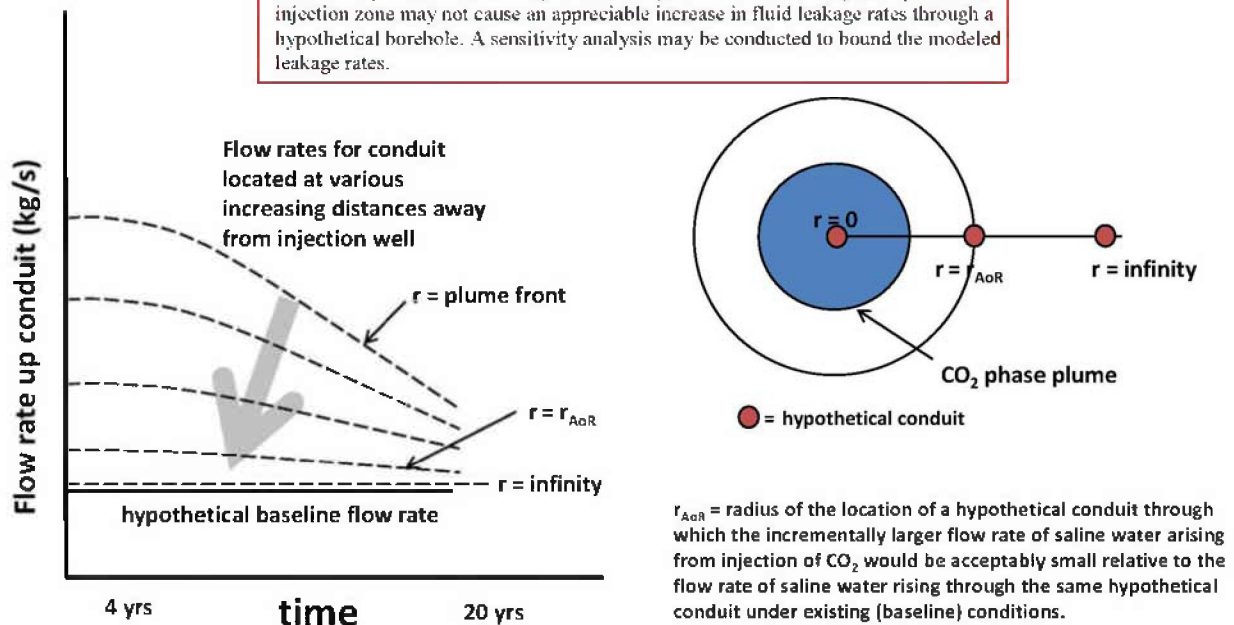
Figure 6.3-1. Summary of approach described in the EPA Class VI revision of May 2013 (USEPA, 2013) describing incremental increase in flow rate arising from injection project relative to baseline (no-injection case) for pre-injection relative overpressure situation. As shown on the left-hand side, the flow rate up the conduit decreases as the distance from the injection well increases. At some distance, the AoR radius, the flow rate for the injection scenario would be larger than the baseline flow rate by an acceptable amount.

Recognizing that the system of interest is primarily one of single-phase injection-induced brine pressurization and upward flow in a borehole, we used previously published analytical solutions (Cihan et al., 2011; 2013) to single-phase flow equations to solve for brine flow up a wellbore at various distances from the injection well, as shown in the schematic of Figure 6.3-2. The goal of these calculations was to estimate flow rates up the well for a range of well locations (distances from the injection well) for injection and no-injection (baseline) cases. These results are then used to make various plots of open-well leakage flow rates for wells located at various locations and to compare these against the no-injection (baseline) cases with wells in the same locations. By this approach, we can understand and compare incremental project-related hypothetical leakage along the lines of the approach outlined in the EPA Class VI 2013 revised guidance (USEPA, 2013).

Parameters for the problem were taken from the 3D flow model for Kevin Dome and are presented in Figure 6.3-2, along with a schematic of the flow problem. Three different values of injection-zone (Duperow) permeability are listed, but here we present results only for a base case (k_{res} = 30 mD). Figure 6.3-3 shows results for two different effective permeabilities of the hypothetical well, 10^8 mD (effectively open hole) in the left-hand-side plot, and 500 mD (fairly permeable wellbore) in the right-hand-side plot. As shown, we included 50 years of baseline leakage (dotted black line) prior to startup of injection. This was done to create a less dynamic

system when injection begins, so that the effects of injection are more easily discernible. As shown, leakage rates are higher for the open-hole (left-hand side) compared to the 500 mD well (right-hand side). Regardless of well conductivity, at the beginning of injection, the leakage rate increases for wells at all locations, but the rate increases faster, the closer the leaky well is to the injection well. Furthermore, the leakage rates are higher, the closer the well is to the injection well. Figure 6.3-4 shows results normalized by the baseline (no-injection) case. For example, in Figure 6.3-4, the incremental brine flow rate up a hypothetical open well into USDW due to the injection project is ~30% higher than the baseline, i.e., if no injection project occurs.

- CO_2 injection rate is 7.921 kg/s for 4 years.
- Assuming the density of CO_2 is 819.3 kg/m³, the equivalent single –phase injection rate is equal to 835.32 m³/d.
- The thickness of the formations between the storage reservoir and the USDW is 172.8 m.

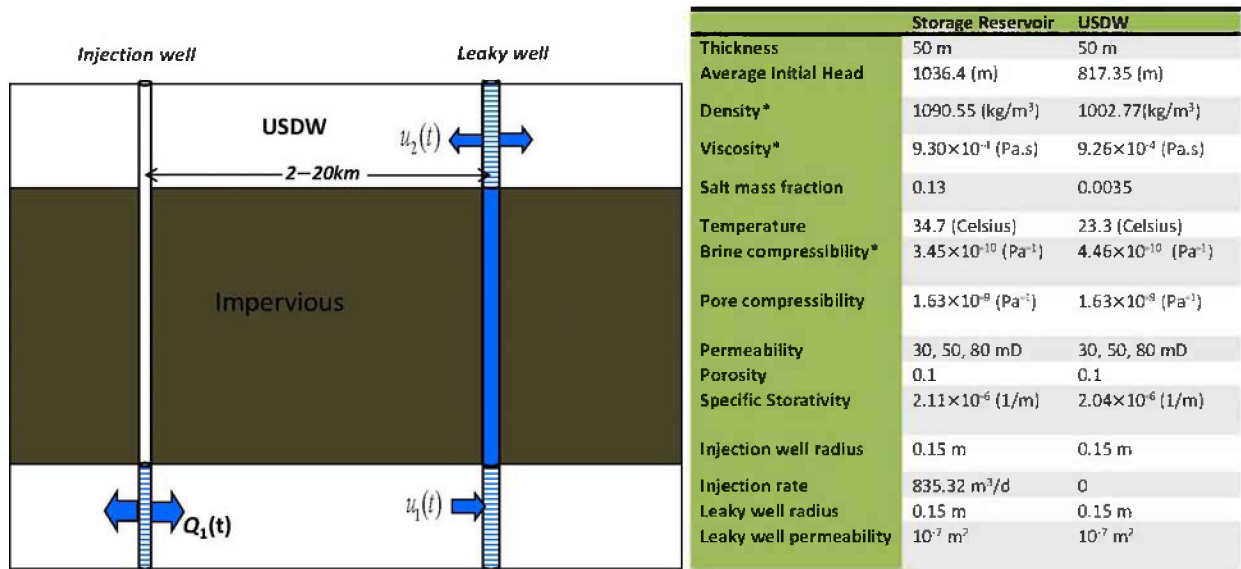|	Storage Reservoir	USDW
Thickness	50 m	50 m
Average Initial Head	1036.4 (m)	817.35 (m)
Density*	1090.55 (kg/m³)	1002.77 (kg/m³)
Viscosity*	9.30×10^{-1} (Pa.s)	9.26×10^{-4} (Pa.s)
Salt mass fraction	0.13	0.0035
Temperature	34.7 (Celsius)	23.3 (Celsius)
Brine compressibility*	3.45×10^{-10} (Pa⁻¹)	4.46×10^{-10} (Pa⁻¹)
Pore compressibility	1.63×10^{-9} (Pa⁻¹)	1.63×10^{-9} (Pa⁻¹)
Permeability	30, 50, 80 mD	30, 50, 80 mD
Porosity	0.1	0.1
Specific Storativity	2.11×10^{-6} (1/m)	2.04×10^{-6} (1/m)
Injection well radius	0.15 m	0.15 m
Injection rate	835.32 m³/d	0
Leaky well radius	0.15 m	0.15 m
Leaky well permeability	10^{-7} m²	10^{-7} m²

Figure 6.3-2. Schematic of the radial flow system for calculating single-phase brine pressurization and flow up a leaky well into USDW, along with assumed injection rate and other parameters.
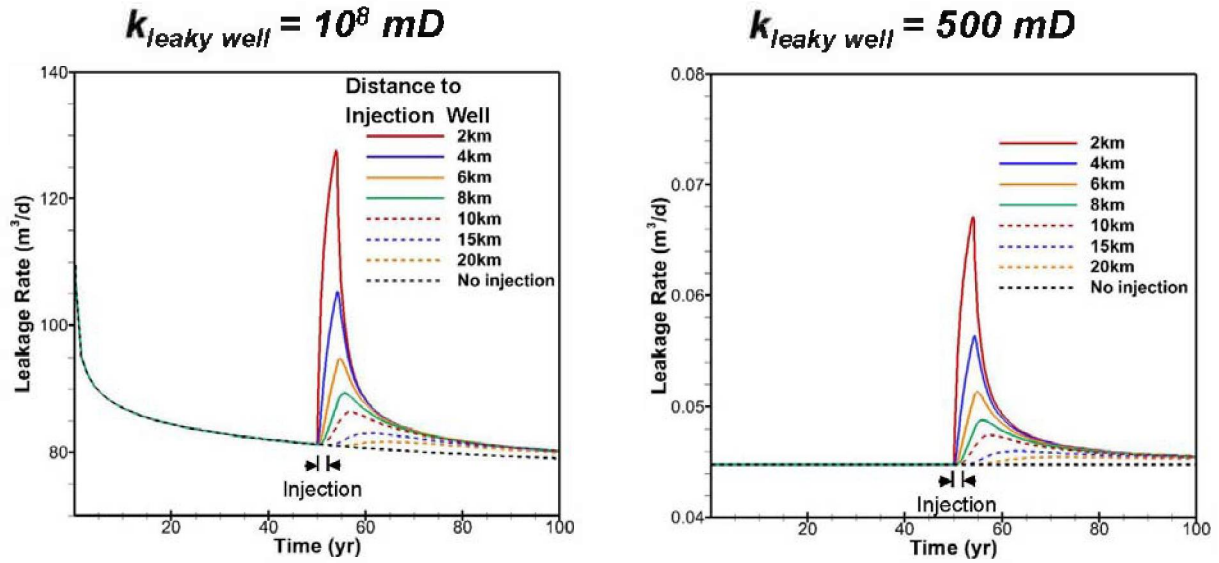
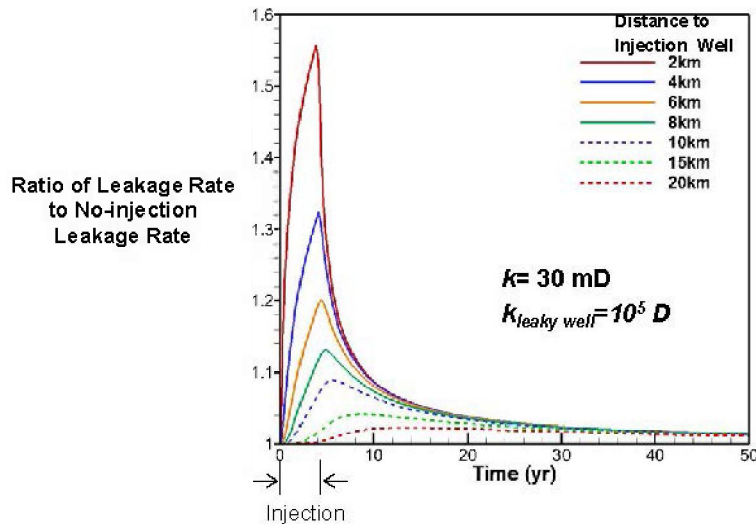**Figure 6.3-3.** *Results of analytical solutions of brine flow from the Duperow to the Madison through hypothetical wells located at various distances from the injection well for two different hypothetical wellbore permeabilities. On the left-hand side, the wellbore has 10^8 mD permeability which makes it effectively an open well.*

Figure 6.3-4. *Normalized brine flow up the well from the Duperow to the Madison through hypothetical wells located at various distances from the injection well.*

Another potential way of evaluating incremental brine leakage into USDW due to injection is to evaluate the incremental total volume of leaked brine. We present, in Figure 6.3-5, two plots of the ratio of total volume of leaked brine for the case of injection, to the total volume of leaked brine for the case of no-injection (baseline). As shown in Figure 6.3-5, the left-hand-side plot shows the incremental leaked volume is at most only a few percent higher than baseline, whereas on the right-hand-side plot, incremental leaked volume is approximately 40% higher than baseline. The reason for this difference is that we have made different assumptions about the total volume of leaked brine in the baseline case. In particular, for the left-hand-side plot, we assume that the baseline brine leakage includes all of the brine leaked over 50 years prior to injection (normalization method 1), whereas on the right-hand-side plot, we assume baseline leakage begins at the onset of injection (normalization method 2). Clearly, the method of normalization to evaluate incremental changes between injection and no-injection (baseline) cases must be carefully considered and defined. We also point out that p. 42 of the EPA Class VI revision only mentions using flow rate and not total leaked volume, so the question about which normalization method of total volume of leaked brine to use may turn out to be moot.

Total volume of leakage normalized by total volume of no-injection (baseline) leakage[1] as a function of time elapsed since the start of the injection

Total volume of leakage normalized by total volume of no-injection (baseline) leakage[2] as a function of time elapsed since the start of the injection

[1]Normalization Method 1: Baseline leakage includes the 50 years prior to injection start.

[2]Normalization Method 2: Baseline leakage starts at start of injection.
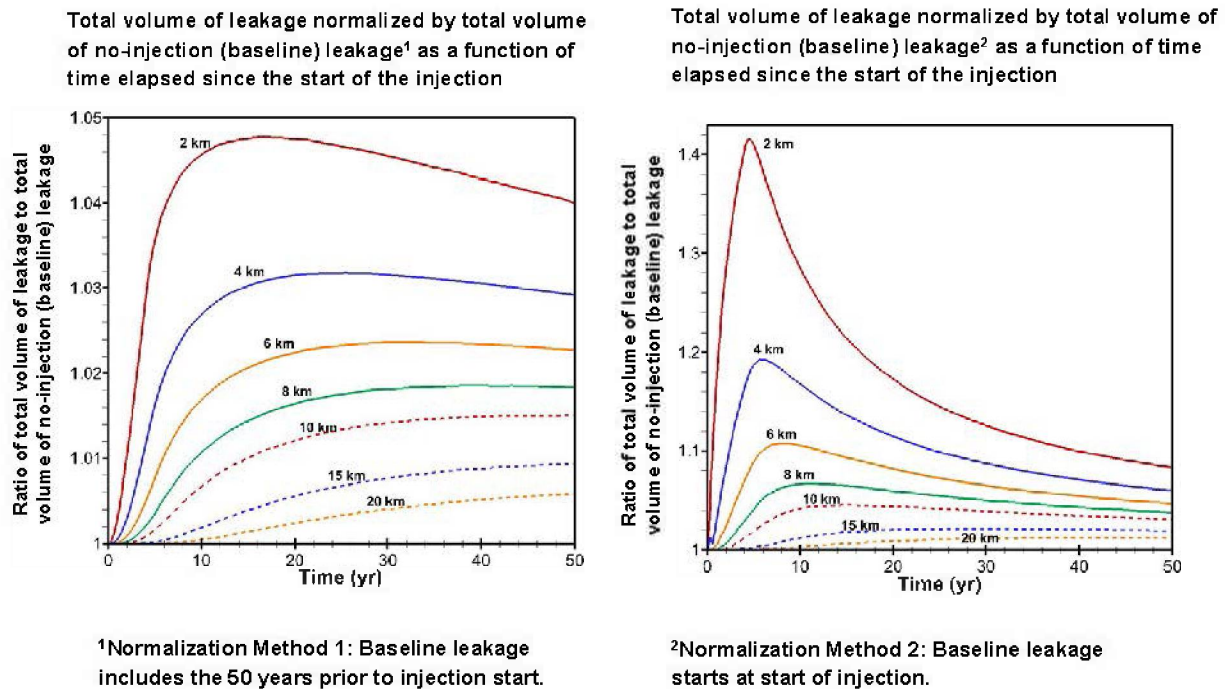
Figure 6.3-5. Instantaneous total volume of leakage normalized by baseline leakage for different well locations as a function of time. In the plot on the left-hand side, the baseline leakage volume is assumed to include 50 years of pre-injection leakage. In the plot on the right-hand side, the baseline leakage volume starts at the time injection starts.

6.4. Conclusions

Because of the apparent pre-injection relative overpressure condition present at Kevin Dome, it appears the project will need to apply the approaches mentioned on p. 42 of the revised EPA Class VI guidance (USEPA, 2013) to arrive at an acceptable AoR. To support the estimation of

AoR, we carried out modeling using published analytical solutions to single-phase flow equations to calculate brine pressurization and associated flow up (single) leaky wells located at a range of distances from the injection well. We find that the incremental flow rates for hypothetical leaky wells located 6 km and 4 km from the injection well are at most approximately 20% and 30% greater, respectively, than hypothetical baseline leakage rates. If total brine leakage is considered, and depending on how incremental total leakage is calculated, we find that incremental total leakage can be either a few percent or up to 40% greater (at most) than baseline total leakage.

ACKNOWLEDGMENTS

REFERENCES

Bénézeth, P., D.A. Palmer, L.M. Anovitz, and J. Horita, 2007. Dawsonite synthesis and reevaluation of its thermodynamic properties from solubilitymeasurements: Implications for mineral trapping of CO_2, *Geochim. Cosmochim.Acta*, 71, 4438–4455.

Bowen, D.W., 2012. Geology of Kevin Dome and implications for CO_2-EOR, Big Sky Carbon Sequestration Partnership Annual Meeting, April 18, 2012, Great Falls, MT.

Brown, A.L., 2012. Update of reservoir Kevin Dome modelling work in progress, Big Sky Carbon Sequestration Partnership Annual Meeting, April 18, 2012, Great Falls, MT.

Carroll, S., E. Mroczek, M. Alai, and M. Ebert, 1998. Amorphous silica precipitation (60 to 120°C): Comparison of laboratory and field Rates, *Geochimica et Cosmochimica Acta*, 62(8), 1379-1396.

Cihan, A., Q. Zhou, and J.T. Birkholzer, 2011. Analytical solutions for pressure perturbation and fluid leakage through aquitards and wells in multilayered-aquifer systems, *Water Resources Research* 47.10, W10504.

Cihan, A., J.T. Birkholzer, and Q. Zhou, 2013. Pressure buildup and brine migration in CO_2 storage systems with multiple leakage pathways: Application of a new analytical solution, *Ground Water*, 51(2), 252–267, DOI:10.1111/j.1745-6584.2012.00972.x

Corey, A.T., 1954. The interrelation between gas and oil relative permeabilities, *Producers Monthly*, 38-41.

Duckworth, O.W. and S.T. Martin, 2004. Role of molecular oxygen in the dissolution of siderite and rhodochrosite, *Geochimica et Cosmochimica Acta*, 68(3), 607–621.

Fatt, I., 1958. Compressibility of sandstones at low to moderate pressure, *AAPG Bull.* 42(8), 1924-1957.

Golubev, S.V., P. Bénézeth, J. Schott, J.L. Dandurand, and A. Castillo, 2009. Siderite dissolution kinetics in acidic aqueous solutions from 25 to 100 °C and 0 to 50 atm P_{CO2}, *Chemical Geology*, 265, 13–19.

Hellevang, H., J. Declercq, B. Kvamme, and P. Aagaard, 2010. The dissolution rates of dawsonite at pH 0.9 to 5 and temperatures of 22, 60 and 77°C, *Appl. Geochem.*, 25, 1575–1586.

Holland, T.J.B. and R. Powell, 1998. An internally consistent thermodynamic dataset for phases of petrological interest, *J. Met. Geol.*, 16, 309–343.

Johnson, J.W, E. Oelkers, H.C. Helgeson, 1992. SUPCRT92: A software package for calculating the standard molal thermodynamic properties of minerals, gases, aqueous species and reactions from 1 to 5000 bar and 0 to 1000°C, *Comput Geosci*, 18, 899–947.

Kharaka Y.K and R.H. Mariner, 1989. Chemical Geothermometers and Their Application to Formation Waters from Sedimentary Basins. Chapter 6 in N. D. Naeser et al. (eds.), *Thermal History of Sedimentary Basins,* Springer-Verlag New York Inc.

Lasaga, A.C., J.M. Soler, J. Ganor, T.E. Burch, and K.L. Nagy, 1994. Chemical weathering rate laws and global geochemical cycles, *Geochim. Cosmochim. Acta,* 58, 2361–2386.

McCutcheon, S.C., J.L. Martin, and T.O. Jr Barnwell, 1993. Water Quality, in Maidment, D.R. (Editor). *Handbood of Hydrology*, McGraw-Hill, New York, NY (p. 11.3)
http://www.earthwardconsulting.com/density_calculator.htm

Palandri, J. and Y.K. Kharaka, 2004. A compilation of rate parameters of water–mineral interaction kinetics for application to geochemical modeling, US Geol. Surv. Open File Report 2004-1068, 64 pp.

Palandri, J. and M.H. Reed, 2001. Reconstruction of *in situ* composition of sedimentary formation waters, *Geochimimica et Cosmochimica Acta*, 65, 1741–1767.

Pan, L., 2003. Wingridder—An interactive grid generator for TOUGH2, paper presented at TOUGH Symposium 2003, Lawrence Berkeley Natl. Lab., Berkeley, Calif., 12 – 14 May.

Pan, L. and C.M. Oldenburg, 2013. T2Well—An integrated wellbore-reservoir simulator, *Computers & Geosciences* (in press).

Pruess, K., 2005. ECO2N: A TOUGH2 fluid property module for mixtures of water, NaCl, and CO$_2$. LBNL-57952, Lawrence Berkeley National Laboratory, Berkeley, CA, USA.

Pruess, K., C. Oldenburg, and G. Moridis, 1999, 2011. TOUGH2 user's guide. Report LBNL-43134-revised, Lawrence Berkeley National Laboratory, Berkeley, CA, USA.

Reed, M.H., 1982. Calculation of multicomponent chemical equilibria and reaction processes in systems involving minerals, gases and an aqueous phase, *Geochimimica et Cosmochimica Acta,* 46, 513–528.

Reed M.H., 1998. Calculation of simultaneous chemical equilibria in aqueous-mineral-gas systems and its application to modeling hydrothermal processes. In: *Techniques in Hydrothermal Ore Deposits Geology, Reviews in Economic Geology*, Volume 10. Richards J, Larson P (eds), 109–124.

Reed M.H. and J. Palandri, 2006. SOLTHERM.H06, a database of equilibrium constants for minerals and aqueous species. Available from the authors, University of Oregon, Eugene, Oregon.

Ryerson, F.J., J. Lake, S. Whittaker, and J.W. Johnson, 2013. Natural CO_2 accumulations in the western Williston Basin: A mineralogical analog for CO_2 injection at the Weyburn site, *International Journal of Greenhouse Gas Control* 16S, S25–S34.

Shepard W., 1991. Tectonics and Thermal Maturation of the Bakken Formation of the Williston Basin, with Comments on Landsat Analysis Applications. Montana Geological Society 2010 - Montana Geological Society: 1991 Guidebook to Geology and Horizontal Drilling of the Bakken Formation, 167-177.

Spycher, N., E. Sonnenthal, and B.M. Kennedy, 2011. Integrating Multicomponent Chemical Geothermometry with Parameter Estimation Computations for Geothermal Exploration. *Geothermal Resources Council Transactions*, 35, 663-666.

Spycher, N., L. Peiffer, and E. Sonnenthal, 2013. GeoT User's Guide A Computer Program for Multicomponent Geothermometry and Geochemical Speciation Version 1.4. Lawrence Berkeley National Laboratory, Report No. LBNL-6172E.
http://esd.lbl.gov/research/projects/geot/

USEPA, 2010. Federal Requirements under the Underground Injection Control (UIC) Program for Carbon Dioxide (CO_2) Geologic Sequestration (GS) Wells. Federal Register, 45(237), 77230-77303.

USEPA, 2013. Underground Injection Control (UIC) Program Class VI Well Area of Review Evaluation and Corrective Action Guidance for Owners and Operators, EPA, Office of Water (4606M), EPA 816-R-13-005, May 2013.

van Genuchten, M. Th., 1980. A closed-form equation for predicting the hydrautic conductivity of unsaturated soils, *Soil Sci. Soc.* 44, 892-898.

Will, R., 2013. Update on the 3D geologic model, Schlumberger Carbon Services, September 23, 2012.

Wilson, J.L., 1967. Carbonate-evaporite cycles in lower Duperow formation of Williston Basin. Bull. *Canadian Petroleum Geology*, 15(3), 230-312.

Xu, T., N. Spycher, E. Sonnenthal, G. Zhang, L. Zheng, and K. Pruess, 2011. TOUGHREACT Version 2.0: A simulator for subsurface reactive transport under non-isothermal multiphase flow conditions, *Computers & Geosciences* 37, 763–774.

Yang, L. and C.I. Steefel, 2008. Kaolinite dissolution and precipitation kinetics at $22^{o}C$ and pH 4. *Geochim. Cosmochim. Ac.*, 72, 99-116.

Zhang, K., Y.S. Wu, and K. Pruess. 2008. User's guide for TOUGH2-MP—A massively parallel version of the TOUGH2 code. Report LBNL-315E, Lawrence Berkeley National Laboratory, Berkeley, CA, USA.